Surfzone to inner-shelf exchange estimated from dye tracer balances

K. Hally-Rosendahl, Integrative Oceanography Division, Scripps Institution of Oceanography, UCSD, 9500 Gilman Dr., La Jolla CA 92093-0209 (kai@coast.ucsd.edu)

F. Feddersen, Integrative Oceanography Division, Scripps Institution of Oceanography, UCSD, 9500 Gilman Dr., La Jolla CA 92093-0209 (falk@coast.ucsd.edu)

D. B. Clark, Woods Hole Oceanographic Institution, MS#12, 266 Woods Hole Rd., Woods Hole, MA 02543 (dclark@whoi.edu)

R. T. Guza, Integrative Oceanography Division, Scripps Institution of Oceanography, UCSD, 9500 Gilman Dr., La Jolla CA 92093-0209 (rguza@ucsd.edu)

Abstract.

Surfzone and inner-shelf tracer dispersion are observed at an approximately alongshore-uniform beach. Fluorescent Rhodamine WT dye, released near the shoreline continuously for 6.5 h, is advected alongshore by breaking wave- and wind-driven currents, and ejected offshore from the surfzone to the inner-shelf by transient rip currents. Novel aerial-based multispectral dye concentration images and in situ measurements of dye, waves, and currents provide tracer transport and dilution observations spanning about 350 m cross-shore and 3 km alongshore. Downstream dilution of near-shoreline dye follows power law decay with exponent -0.33, implying that a 10-fold increase in alongshore distance reduces the concentration about 50%. Coupled surfzone and inner-shelf dye mass balances close, and in 5 h roughly 1/2 of the surfzone-released dye is transported offshore to the inner-shelf. Observed cross-shore transports are parameterized well using a bulk exchange velocity and mean surfzone to inner-shelf dye concentration difference ($r^2 = 0.85$, best fit slope = 0.7). The best fit cross-shore exchange velocity $u^* = 1.2 \times 10^{-2}$ m s^{-1} is similar to a temperature-derived exchange velocity on another day with similar wave conditions. The u^* magnitude and observed inner-shelf dye length scales, time scales, and vertical structure indicate the dominance of transient rip currents in surfzone to inner-shelf cross-shore exchange during moderate waves at this alongshore-uniform beach.

1. Introduction

The nearshore region, consisting of the surfzone (shoreline to x_b, the seaward boundary of depth-limited wave breaking) and the inner-shelf (x_b to approximately 20 m water depth), is vitally important to coastal economies, recreation, and human and ecosystem health. However, nearshore water quality is often compromised by terrestrial runoff and offshore waste disposal [e.g., *Koh and Brooks*, 1975; *Schiff et al.*, 2000; *Halpern et al.*, 2008]. Globally, microbial pathogen exposure from polluted nearshore water causes an estimated 120 million gastrointestinal illnesses and 50 million severe respiratory illnesses annually [*Dorfman and Stoner*, 2012] with significant economic impacts. Furthermore, excess nutrients in polluted runoff can spur rapid growth of harmful algal blooms (HABs), damaging ecosystems and causing serious and even life-threatening human illnesses through direct ocean exposure or consumption of algal-contaminated seafood [*Dorfman and Haren*, 2013].

Pathogens, HABs, and other contaminants are all nearshore tracers; their transport and dilution are governed by surfzone and inner-shelf physical processes. Yet, despite the detriment of contaminated coastal water to our health and economy, understanding of nearshore transport and mixing remains relatively poor. Several field experiments have tracked Lagrangian surface drifters on alongshore-uniform beaches [e.g., *Spydell et al.*, 2007, 2009, 2014] and rip-channeled beaches [e.g., *Brown et al.*, 2009; *MacMahan et al.*, 2010; *Brown et al.*, 2015] to investigate dispersion in the nearshore. Similarly, fluorescent dye [e.g., *Harris et al.*, 1963; *Inman et al.*, 1971; *Grant et al.*, 2005; *Clark et al.*, 2010] has also been used to explore nearshore mixing. However, many of these observations were limited by sparse sampling or small spatio-temporal domains. A rapid-sampling, jetski-based dye measurement platform [*Clark et al.*, 2009] provided improved observation methods. Analyses of dye plume evolution at Huntington Beach, California (HB06) showed that surfzone cross-shore tracer dispersion is dominated by horizontal eddies [*Clark et al.*, 2010; *Feddersen et al.*, 2011; *Clark et al.*, 2011] forced by finite crest length wave breaking [*Peregrine*, 1998; *Spydell and Feddersen*, 2009; *Clark et al.*, 2012; *Feddersen*, 2014]. However, HB06 observations were limited to ≤ 2 hours and usually < 400 m downstream of the dye source, and analyses were specifically restricted to surfzone-contained portions of the dye plumes. While shoreline-source tracers are first transported and mixed within the surfzone, their fate is ultimately determined by exchange with the inner-shelf [e.g., *Hally-Rosendahl et al.*, 2014]. An improved understanding of long time and distance nearshore tracer dilution requires quantitative estimates of net cross-shore surfzone/inner-shelf exchange.

The surfzone and inner-shelf are governed by drastically different dynamics. The surfzone is dominated by breaking-wave-driven currents [e.g., *Thornton and Guza*, 1986] and horizontal eddies [e.g., *Peregrine*, 1998; *Clark et al.*, 2012], whereas the inner-shelf is forced by a combination of wind, tides, buoyancy, and both surface and internal waves [e.g., *Lucas et al.*, 2011; *Lentz and Fewings*, 2012; *Kumar et al.*, 2014; *Sinnett and Feddersen*, 2014]. The intersection of, and exchange between, these dynamically different regions is particularly complex.

The fall 2009 experiment at Imperial Beach, California (IB09) was designed to observe the dispersion of shoreline-released dye with better resolution, for longer times, and over greater cross- and alongshore distances than preceding studies. *Hally-Rosendahl et al.* [2014, hereafter HR14] analyzed 29 September in situ observations across the surfzone and inner-shelf, spanning approximately 7 hours and 700 m alongshore. The 29 Sept mean alongshore current on the inner-shelf was essentially zero. The surfzone was vertically well mixed, while the inner-shelf was strongly stratified immediately offshore of the wave breaking boundary. Horizontal and vertical structure of transient rip current ejection events and the strong stratification limits on inner-shelf vertical mixing were inferred from dye–temperature relationships. Surfzone and inner-shelf alongshore dye dilution followed similar power law decay over 700 m, indicating that inner-shelf dye was locally cross-shore-advected from the surfzone. The power law decay was weaker than previously observed and modeled for dispersion of surfzone-contained dye over shorter times and downstream distances [*Clark et al.*, 2010]. Overall, these observations and analyses suggested that transient rip currents (offshore advection of surfzone eddies) dominated surfzone to inner-shelf cross-shore tracer exchange at alongshore-uniform Imperial Beach [HR14]. However, the cross-shore dye transport could not be measured, and observations were limited to 700 m downstream of the release.

Here, a novel aerial-based dye imaging system [*Clark et al.*, 2014] is used to make high spatial resolution maps of inner-shelf dye spanning > 3 km downstream of a 13 October continuous release. Combined aerial and in situ dye observations across the surfzone and inner-shelf are used to investigate far-downstream dye dilution, surfzone and inner-shelf dye mass balances, and cross-shore dye exchange. These are the first quantitative, coupled surfzone and inner-shelf dye mass balances, and in total 88% of the released dye is accounted for. The IB09 experiment site, dye release, instrument platforms, and sampling schemes are described in section 2. Wave and alongshore current conditions are presented in section 3.1. In section 3.2, the aerial dye observations are described, and time periods and spatial regions for subsequent analyses are established. Surfzone cross-shore and vertical dye structure are described in sections 3.3 and 3.4, respectively. Downstream dye dilution is examined in section 3.5, and alongshore dye transports are presented in section 3.6. Sections 4.1-4.3 present total and regional dye mass balances (with estimation methods described in Appendix A). The closure of these balances allows for observational estimates of surfzone to inner-shelf cross-shore dye transports (section 4.4) which are compared with parameterized estimates in section 5.1. Cross-shore surfzone/inner-shelf exchange mechanisms are discussed in section 5.2. Section 6 is a summary.

2. IB09 Experiment Methods

2.1. Field Site and Coordinate System

IB09 field observations were acquired during fall 2009 at Imperial Beach, California (32.6°N, 117.1°W), a west (269.6°) facing beach with an approximately straight shoreline (Figure 1). In the right-handed coordinate system, cross-shore coordinate x increases negatively seaward ($x = 0$ m at the mean shoreline), alongshore coordinate y increases positively toward the north ($y = 0$ m at the dye release location), and vertical coordinate z increases positively upward ($z = 0$ at mean sea level). The dye release examined here took place on 13 Oct, 2009. Bathymetry surveys from 9 Oct and 19 Oct were similar, and are averaged to give a representative bathymetry for 13 Oct that is approximately alongshore-uniform (Figure 1). All times are in PDT.

2.2. Dye Release

Fluorescent Rhodamine WT dye (2.1×10^8 parts per billion (ppb)) was released continuously at $2.4\ \mathrm{mL\,s^{-1}}$ near the shoreline at $(x, y) = (-10, 0)$ m for approximately 6.5 h

(10:39-17:07 h). Visual observations suggested rapid vertical mixing, and measured dye concentrations were reduced from $O(10^8)$ ppb to $O(10^2)$ ppb within 10 m of the release. Therefore, the dye specific gravity was quickly reduced from 1.2 to ≈ 1. Rhodamine WT has a photochemical decay e-folding time of approximately 667 h of sunlight [e.g., *Smart and Laidlaw*, 1977]; decay over the ≈ 9 h of sunlight during this study is negligible.

2.3. In Situ Instrumentation: Surfzone and Inner-Shelf

2.3.1. Cross-Shore Array

A 125 m-long cross-shore array of six fixed, near-bed instrument frames (denoted f1-f6, onshore to offshore) was deployed from near the shoreline to approximately 4 m water depth (diamonds, Figure 1). The frames held Paros pressure sensors, SonTek acoustic Doppler velocimeters (ADVs), Yellow Springs Instrument Company thermistors, and WET Labs ECO Triplet fluorometers (hereafter ET) to measure dye concentration D. One frame (f4), located near the seaward edge of the surfzone, held instruments at three different vertical locations (0.2, 0.7, and 1.3 m above the bed). Cross-shore array instruments sampled for 51 min each hour, with the remaining 9 min used by the ADVs to estimate bed location [*Feddersen*, 2012; *Spydell et al.*, 2014]. On 13 Oct, the dye release ($y = 0$ m) was 248 m to the south (Figure 1); the alongshore location of this f1-f6 array is denoted by $y_{\mathrm{f}} = 248$ m.

2.3.2. Surfzone Near-Shoreline Alongshore Array

Four thermistor-equipped ETs were deployed near the shoreline at $y = 82, 546, 1069, 1662$ m (circles, Figure 1), referred to as SA1-SA4, respectively. For some analyses, ET data from f2 (at $y_{\mathrm{f}} = 248$ m) are used in conjunction with data from SA1-SA4. The ET on f2 sampled throughout (and after) the dye release, while SA1-SA4 were deployed after the dye release started.

2.3.3. Cross-Shore Jetski Transects

Surface dye concentration and temperature were measured with fluorometers and thermistors mounted on two GPS-tracked jetskis [*Clark et al.*, 2009] that drove repeated cross-shore transects from $x \approx -300$ m to the shoreline (e.g., Figure 1) at various designated alongshore locations between $y = 5$ m and $y \approx 2$ km. The alongshore spacing between transects varied from approximately 20 m (near the release) to 300 m (far downstream of the release). Analyses only include shoreward transects, when jetskis were driven immediately in front of bores to minimize turbidity from bubbles and suspended sand. Seaward transects, sometimes corrupted when jetskis swerved or became airborne jumping over waves, are discarded.

2.3.4. Inner-Shelf Alongshore Boat Transects

Offshore of the surfzone, the vertical and alongshore structure of dye concentration and temperature were measured with a vertical array of five thermistor-equipped ETs towed alongshore behind a small boat. The vertical array sampled from $z = -1$ to -3 m at 0.5 m spacing. During 14:06-17:43 h, repeated ≈ 2 km-long alongshore transects (e.g., Figure 1) were driven at roughly 1 $\mathrm{m\,s^{-1}}$ at a mean cross-shore location nominally twice the surfzone width. The transects were approximately shore-parallel with deviations to avoid large waves.

2.4. Inner-Shelf Dye Aerial Remote Sensing

Novel aerial observations of near-surface dye concentration were obtained from a small plane with a multispectral camera system and coupled global positioning and inertial navigation systems [*Clark et al.*, 2014]. Two cameras captured images near the peak excitation and emission wavelengths of the fluorescent Rhodamine WT. Dye concentrations were determined by calibrating the ratio of emission to excitation radiances with coincident in situ data. Aerial dye concentration errors range from ±1.5 ppb near $D = 0$ ppb to ±4.5 ppb near $D = 20$ ppb. The georeferenced aerial images are combined into mosaics and regridded onto a rectangular grid with 2 m × 2 m lateral resolution. See *Clark et al.* [2014] for details.

Between 11:21 and 15:32 h, 23 mosaic images were obtained, each separated by roughly 6 min (with a longer gap from 13:08 to 14:56 h). The dye field was imaged from the shoreline to roughly 350 m offshore and from the release to roughly 3 km downstream. Pixels with excitation image brightness above an empirical threshold [*Clark et al.*, 2014] owing to sun glitter or white foam from breaking waves are discarded. The surfzone is therefore often poorly resolved, and quantitative analyses of aerial images are confined to the inner-shelf.

2.5. Corrections to Measured Dye Fluorescence

All aerial and in situ dye observations are corrected for temperature per *Smart and Laidlaw* [1977], and all in situ dye observations are corrected for turbidity per *Clark et al.* [2009]. Corrected D typically differ from measured D by less than 5%.

3. Observations

3.1. Wave, Wind, and Alongshore Current Conditions

During the dye release, the incident wave field (with peak period $T_\mathrm{p} = 13$ s) is relatively constant, and the tide varies less than 0.7 m (low tide at 12:33 h). The release-averaged significant wave height $H_s(x)$ shoals to a maximum of 0.87 m at f4 (break point $x_b = -81$ m, mean breaking depth $h_b = 2.1$ m, Figures 2a and 2c). The mean alongshore current $V(x)$ is northward (positive) at all f1-f6 locations, with a near-shoreline maximum of 0.40 $\mathrm{m\,s^{-1}}$ (Figure 2b). Offshore, V decreases to 0.12 $\mathrm{m\,s^{-1}}$ at the seaward surfzone boundary x_b and then increases slightly to 0.17 $\mathrm{m\,s^{-1}}$ at inner-shelf f6 ($x = -135$ m, Figure 2b). The mean surfzone (f1-f4) alongshore current is $V_{SZ} = 0.22$ $\mathrm{m\,s^{-1}}$, and the mean inner-shelf (f4-f6) alongshore current is $V_{IS} = 0.14$ $\mathrm{m\,s^{-1}}$. Wind is from the south at 4-7 $\mathrm{m\,s^{-1}}$.

3.2. Inner-Shelf Surface Dye Evolution

Aerial images (e.g., Figures 3a-3f) spanning 0:42-4:53 h after the $t_0 =$ 10:39 h start of the dye release are partitioned into three time periods based on temporal gaps in images and the dye plume evolution: period I (early-release, 11:21-11:53 h), period II (mid-release, 12:08-13:01 h), and period III (late-release, 14:56-15:32 h). Approximately 40 min after the release begins (Figure 3a, period I), surfzone dye has advected about 600 m alongshore at ≈ 0.25 $\mathrm{m\,s^{-1}}$, consistent with in situ $V_{SZ} = 0.22$ $\mathrm{m\,s^{-1}}$ (Figure 2b). Surfzone dye is ejected onto the inner-shelf in narrow (≈ 50 m) alongshore bands (Figure 3a), presumably due to transient rip currents [e.g., HR14]. As the dye release continues (Figures 3b-3d, period II), the leading portion of inner-shelf dye is alongshore-patchy with length scales ≈ 50 m (as in Figure 3a). Behind the leading edge, slower alongshore advection of inner-shelf dye (e.g., the feature at $y \approx 1250$ m and 1500 m in Figures 3e and 3f, respectively, period III) is apparent at a speed of ≈ 0.15 $\mathrm{m\,s^{-1}}$, consistent with in situ $V_{IS} = 0.14$ $\mathrm{m\,s^{-1}}$ (Figure 2b). At these longer times and downstream distances (Figures 3e and 3f, period III), inner-shelf dye advects alongshore, disperses cross-shore, and moves to larger alongshore length scales. In particular, Figures 3e and 3f reveal a coherent nearshore eddy feature (at $y \approx 1250$ m and 1500 m, respectively) with an alongshore length scale ≈ 300 m, roughly six times larger than the length scales of inner-shelf dye patches when recently ejected from the surfzone (Figure 3; also see Figure 14, which is discussed in detail in section 5.2).

In addition to the temporal partitioning into periods I, II, and III (defined above), the spatial domain is cross-shore-partitioned into the surfzone (SZ) and inner-shelf (IS) regions (separated by $x_b = -81$ m, section 3.1) and alongshore-partitioned into near- and far-field regions A and B (separated by the cross-shore frame array at $y_{\mathrm{f}} = 248$ m, Figure 3a).

The leading alongshore edge of the dye plume $y_{\mathrm{p}}(t)$ is defined as the northernmost location where aerial-imaged inner-shelf D exceeds 3 ppb within 40 m of x_b (green triangles in Figures 3a-3e). The plume leading edge $y_{\mathrm{p}}(t)$ increases roughly linearly during each time period, with the fastest advance during period III (Figure 4a). The $y_{\mathrm{p}}(t)$-associated alongshore velocity averaged over periods I, II, and III is 0.17 $\mathrm{m\,s^{-1}}$ (Figure 4a), and is between the surfzone and inner-shelf means $V_{SZ} = 0.22$ $\mathrm{m\,s^{-1}}$ and $V_{IS} = 0.14$ $\mathrm{m\,s^{-1}}$ observed at the f1-f6 array (Figure 2b and section 3.1).

3.3. Cross-Surfzone Mean Dye Profiles

Time-averaged surface dye profiles $\overline{D}(x, y_j)$ from repeated jetski cross-shore transects at designated alongshore locations y_j are cross- and alongshore-binned corresponding to where near-shoreline dye is released ($y = 0$ m) and measured (SA1, f2, SA2, SA3, and SA4, Figure 1). Near the release ($y = 14$ m), mean dye concentration is high (≈ 80 ppb) near the shoreline and decays to ≈ 10 ppb near x_b (Figure 4b). Immediately downstream ($y = 87$ m), as dye is dispersed offshore, the mean dye cross-surfzone profile begins to flatten. At each alongshore location, the dye standard deviation is $\propto \overline{D}$. Thus, for $y \geq 207$ m, dye is well mixed across the surfzone (Figure 4b), indicating that surfzone-representative D can be estimated using near-shoreline measurements. These observations of dye cross-surfzone uniformity for $y \geq 207$ m are similar to other observational [*Clark et al.*, 2010] and modeling [*Clark et al.*, 2011] results in which the surfzone was well mixed at $y \gtrapprox 200$ m for similar wave and current conditions.

3.4. Surfzone Dye Vertical Structure

Surfzone dye measured at f4 (Figure 2c) is vertically uniform across the three fluorometers (Figure 4c), indicating that the surfzone water column is well mixed by breaking waves. This is consistent with a similar result found during a 29 Sept dye release [HR14], and demonstrates that surfzone dye can be assumed vertically uniform for the purposes of estimating surfzone dye mass and alongshore transport.

3.5. Near-Shoreline Alongshore Dye Dilution

Here, alongshore dye dilution is examined with near-shoreline in situ data from SA1-SA4 and f2 (yellow circles and diamond, respectively, Figure 3). SA1-SA4 were deployed after the dye plume had arrived at their respective locations; data start times (beginning progressively later with downstream distance) indicate instrument deployment times, not plume arrival times (Figure 5). With the exception of SA3 ($y = 1069$ m), SA instruments were recovered shortly after the dye release ended.

When the dye field is roughly stationary, mean near-shoreline dye concentration decays with downstream distance from the release (Figures 5 and 6) because dye is dispersed cross-shore onto the inner-shelf as it is advected alongshore (Figure 3). Near-shoreline dye variability also decreases significantly with y (Figure 5 and vertical bars in Figure 6). For example, near the release at $y = 248$ m, D varies between 0-80 ppb with a mean of 15 ppb, while at $y = 1662$ m, D varies between 4-12 ppb with a mean of 8 ppb (Figures 5b, 5e, and 6). Furthermore, the time scale of dye variability increases with downstream distance from the release (Figures 5a-5e); the characteristic time scale $\left(\overline{(dD/dt)^2}/\overline{D^2}\right)^{-1/2}$ increases monotonically from 71 s at $y = 82$ m to 584 s at $y = 1662$ m. This increasing time scale suggests that characteristic alongshore surfzone dye length scales (≈ 16 m at $y = 82$ m and ≈ 130 m at $y = 1662$ m using $V_{SZ} = 0.22\ \mathrm{m\,s^{-1}}$) also increase with y. This downstream increase in surfzone length scale is qualitatively consistent with the inner-shelf length scale increase (Figures 3a-3f). However, quantitative surfzone and inner-shelf length scale comparison is avoided given the uncertainty in how characteristic tracer length scales evolve with distance from a shoreline boundary.

The near-shoreline mean dye dilutes following a power law,

$$\overline{D} = \overline{D}_0 \left(y/y_0\right)^{\alpha}, \tag{1}$$

where $y_0 = 1$ m is chosen for simplicity. The least squares power law fit has high skill ($r^2 = 0.98$) with best fit constants $\overline{D}_0 = 98(\pm 13)$ ppb and $\alpha = -0.33(\pm 0.02)$ (dashed line in Figure 6). Note that $\alpha = -0.33$ corresponds to relatively weak decay; a 10-fold increase in y reduces $\overline{D}$ by $\approx 50\%$. Power law dilution was also observed during a 29 Sept dye release over shorter distances (700 m) with $\alpha = -0.19$ [HR14]. The power law exponents $\alpha = -0.33$ (observed here) and $\alpha = -0.19$ [HR14] are both smaller than the $\alpha \approx -0.5$ observed and modeled for short (generally ≤ 200 m) portions of dye plumes confined to the surfzone [*Clark et al.*, 2010, 2011]. Note that $\alpha = -0.5$ is only expected for a domain with cross-shore uniform alongshore current and constant eddy diffusivity (i.e., an idealized surfzone, as assumed in *Clark et al.* [2010]), and when the inner-shelf acts as an idealized tracer sink, not recycling any dye back into the surfzone. Once dye disperses seaward of the surfzone onto the inner-shelf, the V_{SZ} and V_{IS} difference, the potential surfzone and inner-shelf diffusivity difference, and the inner-shelf providing an additional dye source to the surfzone [e.g., HR14] each preclude a simple constant-diffusivity Fickian solution ($\alpha = -0.5$) or other simple analytic solution to compare with the observed $\alpha = (-0.19, -0.33)$. The surfzone to inner-shelf cross-shore dye transports and underlying exchange mechanisms that lead to the downstream decay rates observed here are discussed in section 5.

3.6. Alongshore Dye Transport

Dye is advected by the northward alongshore current V (Figures 2b and 3) from the release location $(x, y) = (-10, 0)$ m past the cross-shore array at $y_{\mathrm{f}} = 248$ m. The alongshore dye transport $\mathcal{T}^{y,A/B}$ from region A to region B through y_{f} (Figure 3, diamonds) is estimated for the surfzone,

$$\mathcal{T}_{SZ}^{y,A/B}(t) = \int_{x_b}^{0} d(x,t)V(x,t)D(x,t)\, dx, \tag{2}$$

and the inner-shelf,

$$\mathcal{T}_{IS}^{y,A/B}(t) = \int_{x_{\mathrm{f6}}}^{x_b} d(x,t)V(x,t)D(x,t)\, dx, \tag{3}$$

using in situ, 30 s-averaged total water depth $d = h + \eta$, alongshore current V, and D at f1-f6, assuming vertically uniform $V(x,t)$ and $D(x,t)$. For the surfzone, this assumption is a good approximation (Figure 4c). However, inner-shelf D is not necessarily vertically uniform, as thermal stratification can significantly inhibit inner-shelf vertical dye mixing, even immediately offshore of the vertically mixed surfzone (not shown here, similar to HR14, Figure 15). Inner-shelf V may also be vertically sheared, likely larger in the upper water column, driven by southerly wind. Lastly, dye at y_{f} sometimes extends offshore of f6 (e.g., Figure 3), but V measurements, and therefore the extent of cross-shore integration for (3), are limited to $x_{\mathrm{f6}} = -135$ m. For these reasons, $\mathcal{T}_{IS}^{y,A/B}$ is biased low.

The surfzone and inner-shelf alongshore dye transports $\mathcal{T}_{SZ}^{y,A/B}$ and $\mathcal{T}_{IS}^{y,A/B}$ generally vary between approximately 0-1000 ppb $\mathrm{m^3\,s^{-1}}$ and 0-400 ppb $\mathrm{m^3\,s^{-1}}$, respectively (Figures 7a and 7b). Averaged over the release period, $\overline{\mathcal{T}}_{SZ}^{y,A/B} = 320$ ppb $\mathrm{m^3\,s^{-1}}$ and $\overline{\mathcal{T}}_{IS}^{y,A/B} = 76$ ppb $\mathrm{m^3\,s^{-1}}$, with roughly four times more alongshore dye transport in the surfzone than between f4 and f6. The cumulative (time-integrated) alongshore dye transports at y_{f} for the surfzone and inner-shelf are $\int_{t_0}^{t} \mathcal{T}_{SZ}^{y,A/B}(\tau)\,d\tau$ and $\int_{t_0}^{t} \mathcal{T}_{IS}^{y,A/B}(\tau)\,d\tau$, respectively, where $t_0 =$ 10:39 h is the dye release start time. The cumulative surfzone alongshore transport $\int_{t_0}^{t} \mathcal{T}_{SZ}^{y,A/B}\,d\tau$ is roughly linear during the dye release (Figure 7c) with small steps corresponding to pulses of $\mathcal{T}_{SZ}^{y,A/B}$ (Figure 7a). At $t =$ 18:00 h, after the last of the dye is advected past the cross-shore array, 62% of the total dye released has been alongshore-transported between the shoreline and f4, and at least 15% of the total between f4 and f6 (Figure 7c). Therefore, at least 77% of the total dye released 248 m south of y_{f} is alongshore-transported within $|x_{\mathrm{f6}}| = 135$ m of the shoreline (recall $\mathcal{T}_{IS}^{y,A/B}$ is biased low).

4. Dye Mass Balances and Cross-Shore Exchange

In sections 4.1-4.3, dye mass balances are shown to close in total, for near-field region A and far-field region B, and for the surfzone and inner-shelf. These results are used in section 4.4 to infer the surfzone to inner-shelf cross-shore dye tracer exchange.

4.1. Mass Balance: Total and Regional

Surfzone and inner-shelf dye masses integrated over the entire alongshore domain (regions A ($0 < y \leq 248$ m) and B ($y > 248$ m) combined) are

$$M_{SZ}^{A+B}(t) = \int_{0}^{y_{\mathrm{p}}(t)} \int_{x_b}^{0} \int_{-h}^{0} D(x,y,z,t)\; dz\; dx\; dy, \tag{4}$$

and

$$M_{IS}^{A+B}(t) = \int_{-\infty}^{\infty} \int_{-\infty}^{x_b} \int_{-h}^{0} D(x,y,z,t)\; dz\; dx\; dy, \tag{5}$$

where $y_{\mathrm{p}}(t)$ is the alongshore location of the leading edge of the northward-advecting dye plume (green triangles in Figure 3). Estimation methods for (4) and (5) are described in Appendix A. The total dye mass balance for the surfzone and inner-shelf is

$$M_{SZ}^{A+B}(t) + M_{IS}^{A+B}(t) = \int_{t_0}^{t} Q\; d\tau, \tag{6}$$

where Q is the steady dye release rate, $t_0 = 10{:}39$ h is the dye release start time, and $M_{SZ}^{A+B}(t_0) \equiv M_{IS}^{A+B}(t_0) \equiv 0\ \mathrm{ppb\,m^3}$.

The total dye mass balance (6) closes well over the 11:21-15:32 h time span of aerial images (Figure 8a, compare red asterisks with red line). On average, 88% of the released dye tracer is accounted for using these novel aerial and (relatively sparse) in situ measurements. Note, M_{SZ}^{B} (and therefore M_{SZ}^{A+B}) may be biased low because $y_{\mathrm{p}}(t)$ may be underestimated (Appendix A1). Analyses are broken into time periods I, II, and III based on temporal gaps in aerial data (e.g., Figure 8a) and dye plume evolution (recall section 3.2 and Figure 3). Early in the release during period I, $M_{SZ}^{A+B} \approx M_{IS}^{A+B}$ (Figure 8a). Starting in period II, as more dye spreads from the surfzone to the inner-shelf, M_{IS}^{A+B} becomes larger than M_{SZ}^{A+B}. In period III, $M_{IS}^{A+B} \approx 2M_{SZ}^{A+B}$ (Figure 8a), indicating significant cross-shore transport of surfzone-released dye to the inner-shelf.

The surfzone and inner-shelf are also decomposed into near-field region A and far-field region B (Figure 3a). For the surfzone, $M_{SZ}^{A} \approx M_{SZ}^{B}$ during period I (Figure 8b), when dye has not advected very far downstream (e.g., Figure 3a). As the dye plume advects farther alongshore during period II, M_{SZ}^{B} becomes larger than M_{SZ}^{A}. Though dye concentrations are highest near the release (region A) and decrease downstream, the power law decay is weak (equation (1) and Figure 6), and the larger alongshore extent of the dye plume in region B than region A results in period II $M_{SZ}^{B} \approx 2M_{SZ}^{A}$ (Figure 8b). During period III, dye has advected far downstream (e.g., Figures 3e and 3f), and $M_{SZ}^{B} \approx 4M_{SZ}^{A}$ (Figure 8b). Similar trends are observed for the inner-shelf. During period I, $M_{IS}^{A} \approx M_{IS}^{B}$ (Figure 8c). In period II, M_{IS}^{B} begins to dominate M_{IS}^{A}, and during period III, $M_{IS}^{B} \gg M_{IS}^{A}$ (Figure 8c).

4.2. Mass Balance: Near-field Region A

In near-field region A, the total released dye mass must balance the surfzone and inner-shelf accumulated dye mass and the time-integrated alongshore transport from region A to B:

$$M_{SZ}^{A}(t) + M_{IS}^{A}(t) + \int_{t_0}^{t} \left(\mathcal{T}_{SZ}^{y,A/B} + \mathcal{T}_{IS}^{y,A/B} \right) d\tau = \int_{t_0}^{t} Q \, d\tau. \qquad (7)$$

On average, the sum of the observed region A mass and cumulative A to B transports account for 76% of the released dye (Figure 9a, compare red asterisks with red line). The largest terms of (7) are the cumulative surfzone and inner-shelf alongshore transports, with $\int_{t_0}^{t} \mathcal{T}_{SZ}^{y,A/B} \, d\tau \approx 0.6 \int_{t_0}^{t} Q \, d\tau$ and $\int_{t_0}^{t} \mathcal{T}_{IS}^{y,A/B} \, d\tau \approx 0.2 \int_{t_0}^{t} Q \, d\tau$ during the aerial data time span (Figure 9a, gray and blue curves, respectively). The region A dye masses M_{SZ}^{A} and M_{IS}^{A} are relatively small, especially during period III (Figure 9a, triangles). The 24%

of dye unaccounted for in region A is consistent with the low-bias of $\mathcal{T}_{IS}^{y,A/B}$ (described in section 3.6).

4.3. Mass Balance: Far-field Region B

Similar to the near-field region A, the far-field region B surfzone and inner-shelf accumulated dye mass must balance the time-integrated alongshore transport from A to B:

$$M_{SZ}^{B}(t) + M_{IS}^{B}(t) = \int_{t_0}^{t} \left(\mathcal{T}_{SZ}^{y,A/B} + \mathcal{T}_{IS}^{y,A/B} \right) d\tau. \tag{8}$$

The observed mass and transport estimates agree well, having 18% relative rms error (Figure 9b, compare red circles with red squares), confirming the consistency among aerial and in situ data and the validation of mass and transport estimation methods. On average, the region B accumulated dye mass (red squares, Figure 9b) is slightly larger than the time-integrated alongshore transport (red circles, Figure 9b), again consistent with the low bias of $\mathcal{T}_{IS}^{y,A/B}$ (section 3.6).

4.4. Cross-Shore Surfzone/Inner-Shelf Exchange

Because the section 4.1-4.3 dye mass balances close, cross-shore surfzone to inner-shelf transport estimates for regions A and B ($\mathcal{T}_{SZ/IS}^{x,A}$ and $\mathcal{T}_{SZ/IS}^{x,B}$, respectively) can be inferred from the observations. The region A inner-shelf dye mass must balance cross-shore transport input from the region A surfzone and alongshore transport loss to the region B inner-shelf (Figure 10). The region B inner-shelf dye mass must balance cross-shore transport input from the region B surfzone and alongshore transport input from the region A inner-shelf (Figure 10). The corresponding equations are

$$\int_{t_0}^{t} \mathcal{T}_{SZ/IS}^{x,A}\, d\tau = M_{IS}^{A}(t) + \int_{t_0}^{t} \mathcal{T}_{IS}^{y,A/B}\, d\tau, \tag{9a}$$

$$\int_{t_0}^{t} \mathcal{T}_{SZ/IS}^{x,B}\, d\tau = M_{IS}^{B}(t) - \int_{t_0}^{t} \mathcal{T}_{IS}^{y,A/B}\, d\tau. \tag{9b}$$

Adding (9a) and (9b) yields the expected inner-shelf balance for regions A and B combined:

$$\int_{t_0}^{t} \left(\mathcal{T}_{SZ/IS}^{x,A} + \mathcal{T}_{SZ/IS}^{x,B} \right) d\tau = M_{IS}^{A}(t) + M_{IS}^{B}(t). \tag{10}$$

The total (A+B) inner-shelf-accumulated dye mass must balance the time integral of the total cross-shore transport of surfzone-released dye. The time-integrated cross-shore transports (9a), (9b), and (10) are inferred from the observed inner-shelf dye mass and alongshore transport.

The inferred time-integrated cross-shore transports $\int_{t_0}^{t} \mathcal{T}_{SZ/IS}^{x}\, d\tau$ are approximately linear in each time period, and the associated cross-shore transports $\mathcal{T}_{SZ/IS}^{x}$ are estimated from the slope of each best fit line (Figure 11). The region A cross-shore transport $\mathcal{T}_{SZ/IS}^{x,A}$ is similar for periods I and II (137 and 115 $\mathrm{ppb\,m^3\,s^{-1}}$, respectively), consistent with the fixed 248 m alongshore extent of region A, independent of the dye plume advecting farther northward with time. In contrast, the region B cross-shore transport $\mathcal{T}_{SZ/IS}^{x,B}$ increases significantly among periods I, II, and III (25, 263, and 495 $\mathrm{ppb\,m^3\,s^{-1}}$, respectively) as $y_{\mathrm{p}}(t)$ moves northward (e.g., Figures 3 and 4a). As a result, the region A and B combined cross-shore transport $\mathcal{T}_{SZ/IS}^{x,A+B}$ also increases with time. During period I, when dye has not advected far downstream (e.g., Figure 3a), $\mathcal{T}_{SZ/IS}^{x,A+B} = 162\ \mathrm{ppb\,m^3\,s^{-1}} = 0.32Q$. During period II, when dye has advected farther downstream (e.g., Figures 3b-3d), $\mathcal{T}_{SZ/IS}^{x,A+B} = 378\ \mathrm{ppb\,m^3\,s^{-1}} = 0.74Q$. During period III, when dye has advected approximately 3 km downstream (e.g., Figures 3e and 3f), $\mathcal{T}_{SZ/IS}^{x,A+B} = 498\ \mathrm{ppb\,m^3\,s^{-1}} = 0.97Q$, and most of the cross-shore transport occurs in region B (Figure 11, compare red with green best fit slopes). Over the approximate 5 h of aerial observations, roughly 1/2 of the shoreline-released dye is cross-shore transported to the inner-shelf, i.e., $\int_{t_0}^{t} \mathcal{T}_{SZ/IS}^{x,A+B}\, d\tau \approx \frac{1}{2}\int_{t_0}^{t} Q\, d\tau$ (Figure 11, compare blue symbols with thin red line).

5. Discussion

5.1. Parameterizing Cross-Shore Tracer Exchange

The box-model-based cross-shore tracer flux parameterization used for temperature by HR14 is tested here for dye with the inferred estimates of surfzone to inner-shelf cross-shore dye transport (section 4.4). The cross-shore dye flux $\hat{F}_{SZ/IS}^{x}$ (units $\mathrm{ppb\,m^2\,s^{-1}}$) at the surfzone/inner-shelf boundary x_b is parameterized as

$$\hat{F}_{SZ/IS}^{x} = h_b u^* \Delta\overline{D}, \tag{11}$$

where h_b is the water depth at x_b, u^* is a bulk cross-shore exchange velocity, and $\Delta\overline{D} = \overline{D}_{SZ} - \overline{D}_{IS}$ is the difference between surfzone and inner-shelf mean dye concentrations. Here, $\Delta\overline{D}$ is computed separately for region A and region B and for each time period using period-averaged dye mass estimates $\overline{M}_{SZ}^{A}$, $\overline{M}_{IS}^{A}$, $\overline{M}_{SZ}^{B}$, and $\overline{M}_{IS}^{B}$ (section 4.1) and approximate volumes $\mathcal{V}$ of each region (e.g., $\overline{D}_{SZ}^{A} = \overline{M}_{SZ}^{A}/\mathcal{V}_{SZ}^{A}$). The surfzone volumes are defined by the integration regions for $\overline{M}_{SZ}^{A,B}$ (see Appendix A1). The inner-shelf volumes are estimated using h_{dye} (Appendix A2), cross-shore width $|-250\ \mathrm{m} - x_b| = 169$ m (e.g., Figure 3), and alongshore extents $y_{\mathrm{f}} = 248$ m (region A) and $\overline{y}_{\mathrm{p}} - y_{\mathrm{f}}$ (region B), where $\overline{y}_{\mathrm{p}}$ is the mean of y_{p} for each time period. The parameterized surfzone to inner-shelf cross-shore dye transports $\hat{\mathcal{T}}^{x}_{SZ/IS}$ (units $\mathrm{ppb\,m^3\,s^{-1}}$) are then

$$\hat{\mathcal{T}}^{x,A}_{SZ/IS} = \int_0^{y_\mathrm{f}} \hat{F}^{x,A}_{SZ/IS}\, dy = \int_0^{y_\mathrm{f}} h_b u^* \Delta\overline{D}^{A}\, dy = h_b u^* \Delta\overline{D}^{A} y_\mathrm{f}, \tag{12a}$$

$$\hat{\mathcal{T}}^{x,B}_{SZ/IS} = \int_{y_\mathrm{f}}^{\overline{y}_\mathrm{p}} \hat{F}^{x,B}_{SZ/IS}\, dy = \int_{y_\mathrm{f}}^{\overline{y}_\mathrm{p}} h_b u^* \Delta\overline{D}^{B}\, dy = h_b u^* \Delta\overline{D}^{B} \left(\overline{y}_\mathrm{p} - y_\mathrm{f}\right) \tag{12b}$$

for region A and region B, respectively, and

$$\hat{\mathcal{T}}^{x,A+B}_{SZ/IS} = \hat{\mathcal{T}}^{x,A}_{SZ/IS} + \hat{\mathcal{T}}^{x,B}_{SZ/IS} \tag{13}$$

for regions A and B combined. The parameterized $\hat{\mathcal{T}}^{x,A}_{SZ/IS}$, $\hat{\mathcal{T}}^{x,B}_{SZ/IS}$, and $\hat{\mathcal{T}}^{x,A+B}_{SZ/IS}$ are each computed for periods I, II, and III.

Parameterized $\hat{\mathcal{T}}^{x}_{SZ/IS}$ and inferred $\mathcal{T}^{x}_{SZ/IS}$ are generally similar (Figure 12) with squared correlation $r^2 = 0.85$ and best fit slope 0.7. Minimizing the rms error among parameterized $\hat{\mathcal{T}}^{x}_{SZ/IS}$ and inferred $\mathcal{T}^{x}_{SZ/IS}$ transports yields the best fit bulk cross-shore exchange velocity $u^* = 0.012(\pm 0.001)\ \mathrm{m\,s^{-1}}$. This is consistent with the $u^* = 0.009\ \mathrm{m\,s^{-1}}$ found using temperature observations on another day with similar wave conditions [HR14].

The parameterized $\hat{\mathcal{T}}^{x,A}_{SZ/IS}$ during periods I and II are both similar to the inferred $\mathcal{T}^{x,A}_{SZ/IS}$ (Figure 12, green circle and square), while the period III parameterized $\hat{\mathcal{T}}^{x,A}_{SZ/IS}$ overestimates the small inferred $\mathcal{T}^{x,A}_{SZ/IS}$ (Figure 12, green triangle). The parameterized $\hat{\mathcal{T}}^{x,B}_{SZ/IS}$ increases among periods I, II, and III (Figure 12, vertical coordinates of red symbols) as $y_\mathrm{p}(t)$ moves farther northward (Figure 4a), consistent with the increase of inferred $\mathcal{T}^{x,B}_{SZ/IS}$ (Figure 12, horizontal coordinates of red symbols). Similarly, parameterized $\hat{\mathcal{T}}^{x,A+B}_{SZ/IS}$ and inferred $\mathcal{T}^{x,A+B}_{SZ/IS}$ are comparable, and both increase with time among periods I, II, and III (Figure 12, blue symbols).

During period III, the inferred $\mathcal{T}^{x,A}_{SZ/IS}$ is small (Figure 12, horizontal coordinate of green triangle), suggesting that most of the region A surfzone dye is transported alongshore to the region B surfzone rather than offshore to the inner-shelf. Consistent with this inference, the mean period III surfzone alongshore transport $\overline{\mathcal{T}}_{SZ}^{y,A/B} = 507$ ppb m^3 s^{-1} is within 1% of the dye release rate $Q = 512$ ppb m^3 s^{-1}. Combined with the small M_{IS}^A and $\frac{d}{dt}\left(M_{IS}^A\right)$ during period III (Figure 8c, triangles), this confirms that the period III surfzone to inner-shelf cross-shore transport within region A is small. This is explored further in the next section.

5.2. Surfzone/Inner-Shelf Exchange Mechanisms

The exchange velocity $u^* = 1.2 \times 10^{-2}$ m s^{-1} represents all potential cross-shore surfzone/inner-shelf exchange mechanisms, including rip currents, Stokes drift driven flow, and internal waves. For alongshore-uniform bathymetries, wave-driven cross-shore exchange over the inner-shelf is generally attributed to Stokes drift driven flow [e.g., *Monismith and Fong*, 2004; *Lentz et al.*, 2008; *Lentz and Fewings*, 2012]. Within the vertically well mixed surfzone (e.g., Figure 4c), Stokes drift driven flow was found to be a negligible cross-shore dye dispersion mechanism relative to surfzone eddies [*Clark et al.*, 2010]. However, outside the surfzone on the inner-shelf, vertical dye profiles are not necessarily uniform, and vertically varying Stokes drift driven flow could potentially be an important cross-shore dye exchange mechanism. Here, the u^* magnitude and observed inner-shelf vertical dye profiles are compared with an estimated Stokes drift driven velocity profile offshore of the wave breaking boundary.

Assuming that the near-surface onshore mass flux due to Stokes drift is balanced by a vertically uniform Eulerian return flow yields an estimated Lagrangian (Stokes plus Eulerian; referred to here as Stokes drift driven) velocity profile that is shoreward in the upper water column and seaward at depth. With normally incident, narrow-banded waves (amplitude $a = H_s/(2\sqrt{2})$), the depth-normalized Stokes drift driven seaward velocity appropriate for comparison with u^* is

$$u^*_{\mathrm{s}} = \left| \frac{(ak)^2 C}{2\,(z_0 + h)\sinh^2(kh)} \int_{-h}^{z_0} \left[\cosh\left(2k\,(z+h)\right) - \frac{\sinh\left(2kh\right)}{2kh}\right] dz \right|, \qquad (14)$$

where k is the peak wavenumber, C the phase speed, h the still water depth, and z_0 the vertical location at which the velocity profile switches sign. At f6, the observed $H_s = 0.76$ m (Figure 2a), peak period $T_{\mathrm{p}} = 13$ s, and mean water depth $h = 4.2$ m (Figure 2c) yield $u^*_{\mathrm{s}} = 5.9 \times 10^{-4}\ \mathrm{m\,s^{-1}}$, which is 20× smaller than the inferred exchange velocity $u^* = 1.2 \times 10^{-2}\ \mathrm{m\,s^{-1}}$. Note that if the Eulerian return flow is surface-intensified [e.g., *Putrevu and Svendsen*, 1993; *Lentz et al.*, 2008] instead of depth-uniform, an analogous u^*_{s} is even smaller than estimated by (14).

The estimated Stokes drift driven velocity profile at f6 is also compared with nearby vertical dye profile observations. Time- and alongshore-averaged in situ measurements near $2x_b$ (roughly 25 m offshore of f6, Figure 1) show that the mean inner-shelf dye concentration is surface-intensified and decreases with depth (Figure 13). Because inner-shelf dye is delivered from the vertically mixed surfzone (Figure 4c), the observed inner-shelf mean vertical profiles require seaward dye transport in the upper water column. This is inconsistent with the f6-estimated Stokes drift driven velocity profile which is shoreward in the upper water column and seaward only below $z_0 = -1.8$ m.

Moreover, the observed surfzone to inner-shelf dye ejections are episodic and short-lived ($O(1)$ min) and have small alongshore length scales (O(10-100) m; Figures 3 ($y \leq 1500$ m), 10, and 14), whereas Stokes drift driven exchange is expected to be quasi-stationary and essentially uniform in the alongshore. Similarly, other potential exchange mechanisms such as winds [e.g., *Fewings et al.*, 2008], tides [e.g., *Lentz and Fewings*, 2012], or internal waves [e.g., *Sinnett and Feddersen*, 2014; *Suanda et al.*, 2014] are expected to generally have much larger alongshore length scales and longer time scales than those observed. Farther offshore of the surfzone, Stokes drift driven exchange [e.g., *Lentz et al.*, 2008; *Suanda and Feddersen*, 2015] or other inner-shelf processes may become important. The above differences in exchange velocity magnitude, vertical structure, and time and alongshore length scales indicate that on this day with moderate waves, the observed surfzone to inner-shelf cross-shore dye transport is dominated by rip current ejections.

Here, an example rip current event is highlighted using two of the aerial images (Figure 14). Just offshore of the dye release at t = 12:22 h (Figure 14a), a rip current ejects concentrated ($\geq$ 15 ppb) dye out of the surfzone through a 20 m wide neck, terminating in a roughly 50 m wide rip current head 100 m offshore of the surfzone boundary. Gradients between dye-rich and dye-free water are very strong (Figure 14a). On a subsequent aerial pass (t = 12:35 h, Figure 14b), the ejected dye has advected $\approx$ 150 m alongshore, dispersed to larger spatial scales, and lost its clear rip current signature. Other dye ejections with similar spatial scales and evolution are seen throughout the 23 aerial images (e.g., Figure 3). The observed ejection events are episodic and brief ($O(1)$ min) and occur at random alongshore locations, indicating that these rips are transient and are not bathymetrically controlled, consistent with the approximately alongshore-uniform bathymetry at Imperial Beach (Figure 1). The magnitudes of u^* and $\mathcal{T}^x_{SZ/IS}$ are related to the surfzone eddy field and the frequency and intensity of these transient rip current events, which depend on the incident wave field and beach slope [*Johnson and Pattiaratchi*, 2006; *Suanda and Feddersen*, 2015].

Note that the small $\mathcal{T}_{SZ/IS}^{x,A}$ inferred for region A during period III (Figure 12, green triangle) and the associated lack of significant transient rip ejections (i.e., period III lack of dye in region A inner-shelf, Figures 3e and 3f) are not surprising, as transient rip currents are sporadic in space and time, and region A is small (<250 m alongshore) and period III short (<40 min). Because the cross-shore dye flux (11) is a bulk parameterization and does not resolve the spatial or temporal variability of transient rip ejections, (12a) overpredicts the small cross-shore transport $\mathcal{T}_{SZ/IS}^{x,A}$ observed during period III for region A. However, the period III parameterized $\hat{\mathcal{T}}_{SZ/IS}^{x,A+B}$ still agrees well with the observed $\mathcal{T}_{SZ/IS}^{x,A+B}$ for the full alongshore domain (regions A+B; Figure 12, blue triangle).

6. Summary

A continuous 6.5 h, near-shoreline release of fluorescent Rhodamine WT dye tracer was observed on 13 October, 2009, at the alongshore-uniform Imperial Beach, California (IB09 experiment). Surfzone and inner-shelf dye concentrations were measured in situ with fixed and mobile (jetski- and boat-mounted) fluorometers, and remotely with a novel aerial-based multispectral camera system. Waves and currents were measured between the shoreline and roughly 4 m water depth. Dye was advected alongshore by breaking wave- and wind-driven currents, forming a several km long plume.

Aerial images showed the plume advecting alongshore at rates consistent with in situ observations while transient rip currents intermittently transported surfzone dye to the inner-shelf via brief ($O(1)$ min) and narrow ($O(10)$ m) seaward ejections at random alongshore locations. Once on the inner-shelf, the ejected dye patches continued to advect (less quickly) alongshore while dispersing to larger cross- and alongshore length scales. At a cross-shore instrument array 248 m downstream of the release location, 77% of the released dye was alongshore-advected through the array within roughly two surfzone widths of the shoreline.

Alongshore dye dilution power law exponents -0.33 (observed here over ≈ 2 km) and -0.19 (on 29 Sept over ≈ 700 m, HR14) are both smaller than -0.5 previously found for surfzone-contained dye plumes over much shorter (≤ 200 m) downstream distances before dye leaked offshore to the inner-shelf [*Clark et al.*, 2010, 2011]. This deviation of the long distance power law exponents ($-0.33, -0.19$) from the short distance, surfzone-only exponent (-0.5) highlights the complexity of the coupled surfzone/inner-shelf domain and the governing dynamical processes.

A combination of aerial and in situ measurements were used to calculate the first coupled surfzone and inner-shelf dye mass balances. On average, 88% of the total released dye mass was accounted for across the surfzone and inner-shelf (≈ 350 m cross-shore and 3 km alongshore) over a 5 h period during the release. Dye mass and alongshore transport observations for separate near- and far-field regions were also in agreement, and the small discrepancies were consistent with low-biased inner-shelf alongshore transport measurements. The closure of these dye mass balances allowed for quantitative observational estimates of surfzone to inner-shelf cross-shore dye transports, which amounted to roughly 1/2 of the shoreline-released dye during the same 5 h period.

The observed cross-shore dye transports were parameterized well (correlation $r^2 = 0.85$, best fit slope 0.7) using a bulk exchange velocity and surfzone/inner-shelf mean dye concentration difference. The resulting best fit bulk exchange velocity $u^* = 1.2 \times 10^{-2}$ m s^{-1} is consistent with a temperature-derived exchange velocity from another day with similar waves. An estimated Stokes drift driven velocity is $20\times$ smaller than u^* and has a vertical profile that is inconsistent with the observed inner-shelf mean vertical dye structure. Other potential cross-shore exchange mechanisms (e.g., winds, tides, internal waves) are expected to generally have spatio-temporal scales much larger than the alongshore-narrow ($O(10-100)$ m) and short-lived ($O(1)$ min) rip current events observed here. These differences suggest that the transient rip current ejections observed at this alongshore-uniform beach dominated the cross-shore surfzone to inner-shelf tracer exchange during moderate wave conditions.

Appendix A: Dye Mass Estimates

A1. Surfzone

The total surfzone dye mass in regions A and B is defined as

$$M_{SZ}^{A+B}(t) = \int_0^{y_{\mathrm{p}}(t)} \int_{x_b}^0 \int_{-h}^0 D(x, y, z, t)\, dz\, dx\, dy, \tag{A1}$$

where h is the water depth, x_b is the seaward surfzone boundary, and $y_{\mathrm{p}}(t)$ is the location of the leading alongshore edge of the northward-advecting dye plume (Figures 3 and 4a; explicit definition in section 3.2). The surfzone dye mass is estimated at times corresponding to the aerial images. The three M_{SZ} integrals (dz, dx, dy) are estimated as follows. Dye is vertically well mixed in the surfzone (Figure 4c and HR14), and therefore the vertical integral becomes

$$\int_{-h}^0 D(x, y, z, t)\, dz = hD(x, y, t). \tag{A2}$$

Cross-shore D profiles do not exist for all y and t. However, cross-shore jetski transects were repeated at various y and are used to compute time-averaged cross-shore dye profiles (see section 3.3 and Figure 4b) at alongshore locations near f2 and SA1-SA4, where near-shoreline dye was measured continuously. These mean profiles are used to compute a surfzone dye cross-shore uniformity parameter $\xi(y)$ defined as

$$\xi(y) = \frac{\int_{x_b}^{0} h(x)\overline{D}(x,y)dx}{\overline{h}_{\mathrm{SZ}}|x_b|\overline{D}(x \approx -10 \text{ m}, y)}, \tag{A3}$$

where $\overline{h}_{\mathrm{SZ}}$ is the mean surfzone water depth, and $x \approx -10$ m is the location of the shoreward-most observations. By definition $0 < \xi(y) \leq 1$, with $\xi \approx 0$ corresponding to shoreline-released dye being highly shoreline-concentrated and $\xi = 1$ corresponding to dye being perfectly cross-shore uniform. Close to the dye release ($y = 14$ m), the cross-shore uniformity parameter $\xi \approx 0.5$. Downstream, as dye mixes across the surfzone, ξ increases to > 0.9 by $y = 810$ m (Figure 15). The cross-shore integral is estimated as

$$\int_{x_b}^{0} h(x)\; D(x,y,t)\; dx = \overline{h}_{\mathrm{SZ}}|x_b|\xi(y) D_{\mathrm{sl}}(y,t), \tag{A4}$$

where $D_{\mathrm{sl}}(y,t)$ is dye measured near the shoreline. Combining (A1)-(A4) yields

$$M_{SZ}^{A+B}(t) = \int_{0}^{y_{\mathrm{p}}(t)} \overline{h}_{SZ}|x_b|\xi(y) D_{\mathrm{sl}}(y,t)\; dy. \tag{A5}$$

The integral (A5) is alongshore-integrated numerically using the trapezoid rule with $D_{\mathrm{sl}}(y,t)$ at $y = 1$ m, y_{SA1}, y_{f}, y_{SA2}, y_{SA3}, y_{SA4}, and $y_{\mathrm{p}}(t)$ (Figure 3, yellow symbols and green triangle). Nearest the release, $D_{\mathrm{sl}}(y = 1 \text{ m}, t) = 98$ ppb is estimated via the best-fit (1) (see Figure 6) during times that dye is being released (note that all M estimates are during the release period). Downstream, $D_{\mathrm{sl}}(y_{\mathrm{p}}(t), t)$ is also estimated using the best-fit (1) (see Figures 4a and 6).

$M_{SZ}^{A+B}(t)$ are decomposed into $M_{SZ}^{A}(t)$ ($0 \leq y < y_{\mathrm{f}}$) and $M_{SZ}^{B}(t)$ ($y_{\mathrm{f}} \leq y \leq y_{\mathrm{p}}(t)$) using the alongshore boundary $y_{\mathrm{f}} = 248$ m. M_{SZ} estimates are computed for all aerial image times when in situ near-shoreline dye data are available. Note that $M_{SZ}^{B}(t)$ and

$M_{SZ}^{A+B}(t)$ may be biased low because $y_{\mathrm{p}}(t)$ (defined as the northernmost location where aerial-imaged inner-shelf D exceeds 3 ppb within 40 m of x_b; green triangles in Figures 3a-3e) may be smaller than the actual extent of the dye plume within the surfzone (where the alongshore current is fastest (Figure 2b)) and the transient rips that eject dye from the surfzone to the inner-shelf are sporadic in space and time.

A2. Inner-Shelf

The total inner-shelf dye mass in regions A and B is defined as

$$M_{IS}^{A+B}(t) = \int_{-\infty}^{\infty}\int_{-\infty}^{x_b}\int_{-h}^{0} D(x,y,z,t)\;dz\;dx\;dy, \qquad \text{(A6)}$$

where h is the still water depth, and x_b is the surfzone/inner-shelf boundary. Inner-shelf dye mass estimates are calculated using surface dye concentration maps $D_s(x,y,t)$ from the aerial images (e.g., Figure 3) and in situ observations of inner-shelf vertical dye structure (Figure 13) from the boat-towed vertical array (section 2.3.4). The towed array data resolve inner-shelf D for $z = -1$ to -3 m, thus requiring assumptions for the vertical structure outside this range. As inner-shelf dye comes from the vertically mixed surfzone (Figure 4c and HR14), inner-shelf $D(x,y,z,t)$ is assumed vertically uniform in the upper 1 m. For $z < -3$ m, the best fit of mean $\overline{D}(z)$ (Figure 13) is extrapolated to the depth where it would vanish. This structure is then vertically integrated, and h_{dye} is computed as the depth that yields an equivalent vertical integral $h_{\mathrm{dye}}D_s(x,y,t)$. The inner-shelf vertical dye integral is thus estimated as

$$\int_{-h}^{0} D(x,y,z,t)\;dz = h_{\mathrm{dye}}D_s(x,y,t), \qquad \text{(A7)}$$

where $D_s(x,y,t)$ is the aerial-measured surface dye concentration, and $h_{\mathrm{dye}} = \min(2.67\text{ m},\, h)$. The inner-shelf dye mass estimates are then

$$M_{IS}^{A+B}(t) = \int_{-\infty}^{\infty}\int_{-\infty}^{x_b} h_{\mathrm{dye}} D_s(x,y,t)\, dx\, dy, \qquad \text{(A8)}$$

integrated using the trapezoid rule in each lateral direction. $M_{IS}^{A+B}(t)$ are decomposed into $M_{IS}^{A}(t)$ $(0 \le y < y_{\mathrm{f}})$ and $M_{IS}^{B}(t)$ $(y_{\mathrm{f}} \le y < \infty)$ using the alongshore boundary $y_{\mathrm{f}} = 248$ m.

Acknowledgments.

IB09 field work and analysis was funded by ONR, NSF, and California Sea Grant. K. Hally-Rosendahl was supported by the National Science Foundation Graduate Research Fellowship under Grant No. DGE1144086 and California Sea Grant under Project No. R/CONT-207TR. Staff and students from the Integrative Oceanography Division (B. Woodward, B. Boyd, K. Smith, D. Darnell, R. Grenzeback, A. Gale, M. Spydell, M. Omand, M. Yates, M. Rippy, A. Doria) were instrumental in acquiring the field observations. K. Millikan, D. Ortiz-Suslow, M. Fehlberg, and E. Drury provided field assistance. Imperial Beach lifeguards, supervised by Captain R. Stabenow, helped maintain public safety. The YMCA Surf Camp management generously allowed extensive use of their facility for staging and recuperation. The U. S. Navy provided access to Naval property for data collection. Dr. M. Okihiro coordinated permits and logistics. We thank these people and organizations. This work comprises a portion of K. Hally-Rosendahl's PhD thesis. As subsequent thesis chapters will use these same IB09 data, they are not shared with this work. However, upon completion of K. Hally-Rosendahl's thesis, IB09 data will be made available at http://falk.ucsd.edu in accordance with the AGU data policy.

References

Brown, J., J. MacMahan, A. Reniers, and E. Thornton (2009), Surf zone diffusivity on a rip-channeled beach, *J. Geophys. Res.*, *114*, doi:10.1029/2008JC005158.

Brown, J. A., J. H. MacMahan, A. J. H. M. Reniers, and E. B. Thornton (2015), Field observations of surf zone-inner shelf exchange on a rip-channeled beach, *J. Phys. Ocean.*, doi:10.1175/JPO-D-14-0118.1, in press.

Clark, D. B., F. Feddersen, M. M. Omand, and R. T. Guza (2009), Measuring fluorescent dye in the bubbly and sediment laden surfzone, *Water Air Soil Poll.*, doi: 10.1007/s11270-009-0030-z.

Clark, D. B., F. Feddersen, and R. T. Guza (2010), Cross-shore surfzone tracer dispersion in an alongshore current, *J. Geophys. Res.*, *115*(C10035), doi:10.1029/2009JC005683.

Clark, D. B., F. Feddersen, and R. T. Guza (2011), Modeling surfzone tracer plumes, part 2: Transport and dispersion, *J. Geophys. Res., Oceans*, *116*(C11028), doi: 10.1029/2011JC007211.

Clark, D. B., S. Elgar, and B. Raubenheimer (2012), Vorticity generation by short-crested wave breaking, *Geophys. Res. Lett.*, *39*, doi:10.1028/2012GL054034.

Clark, D. B., L. Lenain, F. Feddersen, E. Boss, and R. T. Guza (2014), Aerial imaging of fluorescent dye in the nearshore, *J. Atmos. and Ocean. Tech.*, *31*, 1410–1421, doi: 10.1175/JTECH-D-13-00230.1.

Dorfman, M., and A. Haren (2013), Testing the Waters: A guide to water quality at vacation beaches, *Tech. rep.*, National Resources Defense Council.

Dorfman, M., and N. Stoner (2012), Testing the Waters: A guide to water quality at vacation beaches, *Tech. rep.*, National Resources Defense Council.

Feddersen, F. (2012), Scaling surfzone dissipation, *Geophys. Res. Lett.*, *39*(L18613), doi: 10.1029/2012GL052970.

Feddersen, F. (2014), The generation of surfzone eddies in a strong alongshore current, *J. Phys. Ocean.*, *44*, 600–617, doi:10.1175/JPO-D-13-051.1.

Feddersen, F., D. B. Clark, and R. T. Guza (2011), Boussinesq modeling of surfzone tracer plumes, Part 1: Eulerian wave and current comparisons, *J. Geophys. Res.*, *116*(C11027), doi:10.1029/2011JC007210.

Fewings, M., S. J. Lentz, and J. Fredericks (2008), Observations of cross-shelf flow driven by cross-shelf winds on the inner continental shelf, *J. Phys. Ocean.*, *38*(11), 2358–2378, doi:10.1175/2008JPO3990.1.

Grant, S. B., J. H. Kim, B. H. Jones, S. A. Jenkins, J. Wasyl, and C. Cudaback (2005), Surf zone entrainment, along-shore transport, and human health implications of pollution from tidal outlets, *J. Geophys. Res.*, *110*(C10025), doi:10.1029/2004JC002,401.

Hally-Rosendahl, K., F. Feddersen, and R. T. Guza (2014), Cross-shore tracer exchange between the surfzone and inner-shelf, *Journal of Geophysical Research: Oceans*, *119*(7), 4367–4388, doi:10.1002/2013JC009722.

Halpern, B. S., S. Walbridge, K. A. Selkoe, C. V. Kappel, F. Micheli, C. D'Agrosa, J. F. Bruno, K. S. Casey, C. Ebert, H. E. Fox, R. Fujita, D. Heinemann, H. S. Lenihan, E. M. P. Madin, M. T. Perry, E. R. Selig, M. Spalding, R. Steneck, and R. Watson (2008), A global map of human impact on marine ecosystems, *SCIENCE*, *319*(5865), 948–952, doi:10.1126/science.1149345.

Harris, T. F. W., J. M. Jordaan, W. R. McMurray, C. J. Verwey, and F. P. Anderson (1963), Mixing in the surf zone, *Int. J. Air Wat. Polut.*, *7*, 649–667.

Inman, D. L., R. J. Tait, and C. E. Nordstrom (1971), Mixing in the surf zone, *J. Geophys. Res.*, *26*, 3493–3514.

Johnson, D., and C. Pattiaratchi (2006), Boussinesq modelling of transient rip currents, *Coastal Eng.*, *53*(5), 419–439.

Koh, R., and N. Brooks (1975), Fluid mechanics of waste-water disposal in the ocean, in *Annual review of fluid mechanics. Vol.7*, edited by M. Van Dyke and G. Vincenti, pp.

187–211.

Kumar, N., F. Feddersen, J. C. McWilliams, Y. Uchiyama, and W. O'Reilly (2014), Mid-shelf to surf zone coupled ROMS-SWAN model-data comparison of waves, currents, and temperature: Diagnosis of subtidal forcings and response, *J. Phys. Ocean.*, *45*(6), 1464–1490, doi:10.1175/JPO-D-14-0151.1.

Lentz, S. J., and M. R. Fewings (2012), The Wind- and Wave-Driven Inner-Shelf Circulation, *4*, 317–343, doi:10.1146/annurev-marine-120709-142745.

Lentz, S. J., M. Fewings, P. Howd, J. Fredericks, and K. Hathaway (2008), Observations and a model of undertow over the inner continental shelf, *J. Phys. Ocean.*, *38*(11), 2341–2357, doi:10.1175/2008JPO3986.1.

Lucas, A., P. Franks, and C. Dupont (2011), Horizontal internal-tide fluxes support elevated phytoplankton productivity over the inner continental shelf, *Limnology and Oceangraphy: Fluids and Environment*, *1*, 56–74, doi:10.1215/21573698-1258185.

MacMahan, J., J. Brown, J. Brown, E. Thornton, A. Reniers, T. Stanton, M. Henriquez, E. Gallagher, J. Morrison, M. J. Austin, T. M. Scott, and N. Senechal (2010), Mean Lagrangian flow behavior on an open coast rip-channeled beach: A new perspective, *Marine Geology*, *268*(14), 1 – 15, doi:10.1016/j.margeo.2009.09.011.

Monismith, S. G., and D. A. Fong (2004), A note on the potential transport of scalars and organisms by surface waves, *Limnology and Oceanography*, *49*(4), 1214–1217.

Peregrine, D. H. (1998), Surf zone currents, *Theor. Comput. Fluid Dyn.*, *10*, 295–309.

Putrevu, U., and I. A. Svendsen (1993), Vertical structure of the undertow outside the surf zone, *J. Geophys. Res.*, *98*(C12), 22,707–22,716, doi:10.1029/93JC02399.

Schiff, K. C., M. J. Allen, E. Y. Zeng, and S. M. Bay (2000), Southern California, *Mar. Polut. Bull.*, *41*, 76–93.

Sinnett, G., and F. Feddersen (2014), The surf zone heat budget: The effect of wave heating, *Geophysical Research Letters*, *41*(20), 7217–7226, doi:10.1002/2014GL061398.

Smart, P. L., and I. M. S. Laidlaw (1977), An evaluation of some fluorescent dyes for water tracing, *Water Resources Research*, *13*(1), 15–33.

Spydell, M., F. Feddersen, R. T. Guza, and W. E. Schmidt (2007), Observing surfzone dispersion with drifters, *J. Phys. Ocean.*, *27*, 2920–2939.

Spydell, M. S., and F. Feddersen (2009), Lagrangian drifter dispersion in the surf zone: Directionally spread, normally incident waves, *J. Phys. Ocean.*, *39*, 809–830.

Spydell, M. S., F. Feddersen, and R. T. Guza (2009), Observations of drifter dispersion in the surfzone: The effect of sheared alongshore currents, *J. Geophys. Res.*, *114*(C07028), doi:10.1029/2009JC005328.

Spydell, M. S., F. Feddersen, J. H. MacMahan, and R. T. Guza (2014), Relating Lagrangian and Eulerian horizontal eddy statistics in the surf zone, *J. Geophys. Res.*, *119*, doi:10.1002/2013JC009415.

Suanda, S. H., and F. Feddersen (2015), Self-similar scaling for cross-shelf exchange by transient rip currents, *Geophysical Research Letters*, in press.

Suanda, S. H., J. A. Barth, R. A. Holman, and J. Stanley (2014), Shore-based video observations of nonlinear internal waves across the inner shelf, *Journal of Atmospheric and Oceanic Technology*, *31*(3), 714–728, doi:10.1175/JTECH-D-13-00098.1.

Thornton, E. B., and R. T. Guza (1986), Surf zone longshore currents and random waves: Field data and models, *J. Phys. Ocean.*, *16*(7), 1165–1178.

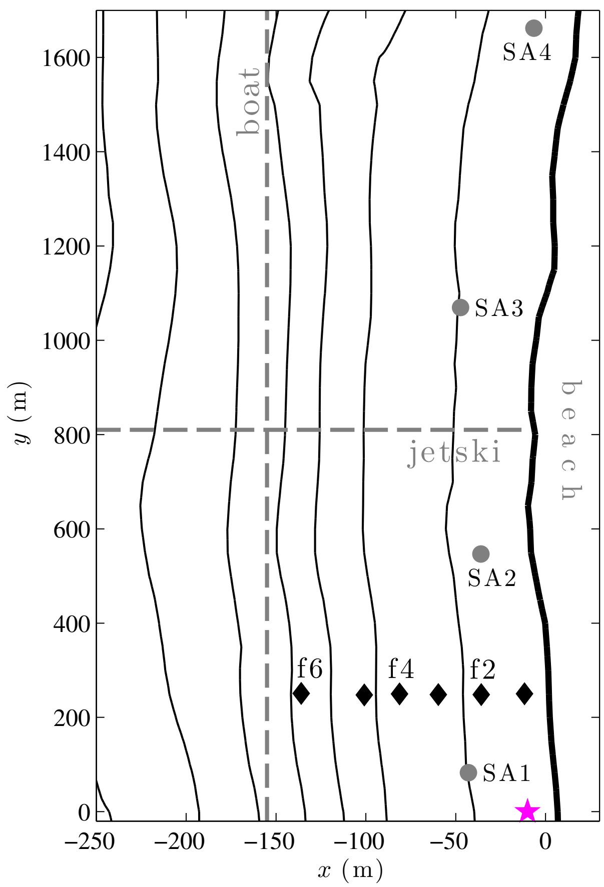

Figure 1. Planview of IB09 bathymetry contours versus cross-shore coordinate x and alongshore coordinate y. Star indicates dye release location. Diamonds denote the cross-shore array of bottom-mounted instrument frames f1-f6 (onshore to offshore). Circles indicate SA1-SA4 fluorometer locations. Vertical dashed line represents an idealized boat alongshore transect driven repeatedly near this cross-shore location. Horizontal dashed line represents an idealized jetski cross-shore surface transect driven repeatedly at various alongshore locations.

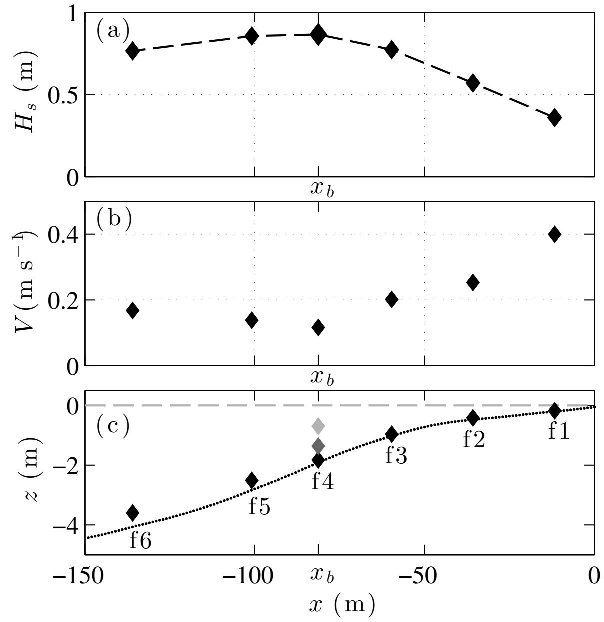

Figure 2. Time-averaged (11:00-16:00 h) (a) significant wave height H_s, (b) alongshore current V, and (c) vertical locations of f1-f6 versus cross-shore coordinate x. In (c), the black curve gives the bathymetry $h(x)$. The mean seaward surfzone boundary $x_b = -81$ m is defined as the location of maximum H_s.

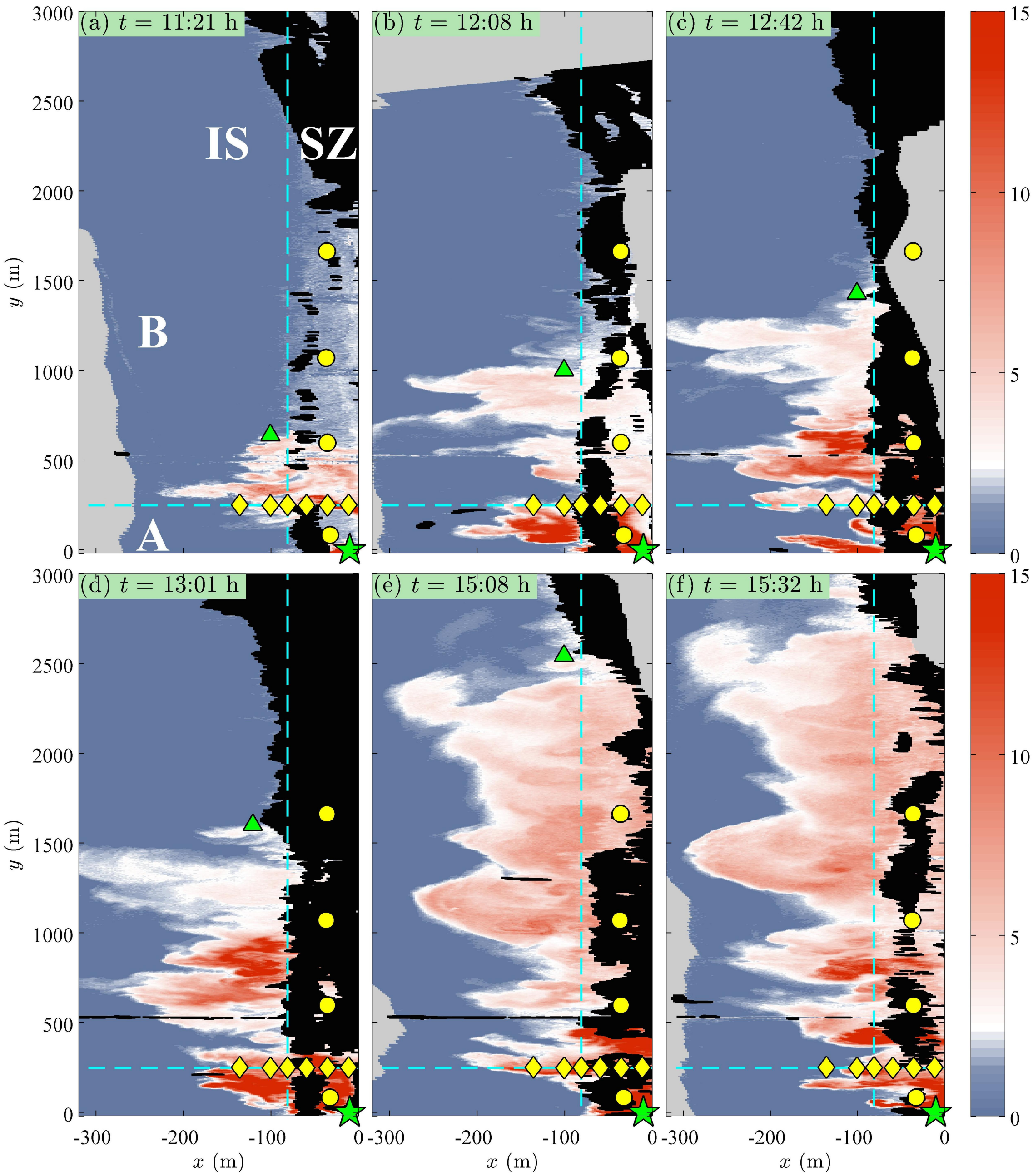

Figure 3. Aerial multispectral images of surface dye concentration D (ppb, see colorbar) versus cross-shore coordinate x and alongshore coordinate y for six times (indicated in each panel). The mean shoreline is at $x = 0$ m. Green star indicates location of continuous dye release (starting at $t_0 = 10{:}39$ h). Yellow diamonds indicate cross-shore array f1-f6 locations, and yellow circles indicate SA1-SA4 locations. Light gray indicates regions outside the imaged area, and black indicates unresolved regions due to foam from wave breaking. Vertical dashed cyan line at x_b divides the surfzone (SZ) and inner-shelf (IS), and horizontal cyan line divides the near- and far-field regions A and B (see panel (a)). Plume leading edge $y_{\mathrm{p}}(t)$ is shown with green triangles at $x \approx -100$ m (for panel (f), $y_{\mathrm{p}} \approx 3250$ m). Panels (a), (b)-(d), and (e)-(f) are in time periods I, II, and III, respectively.

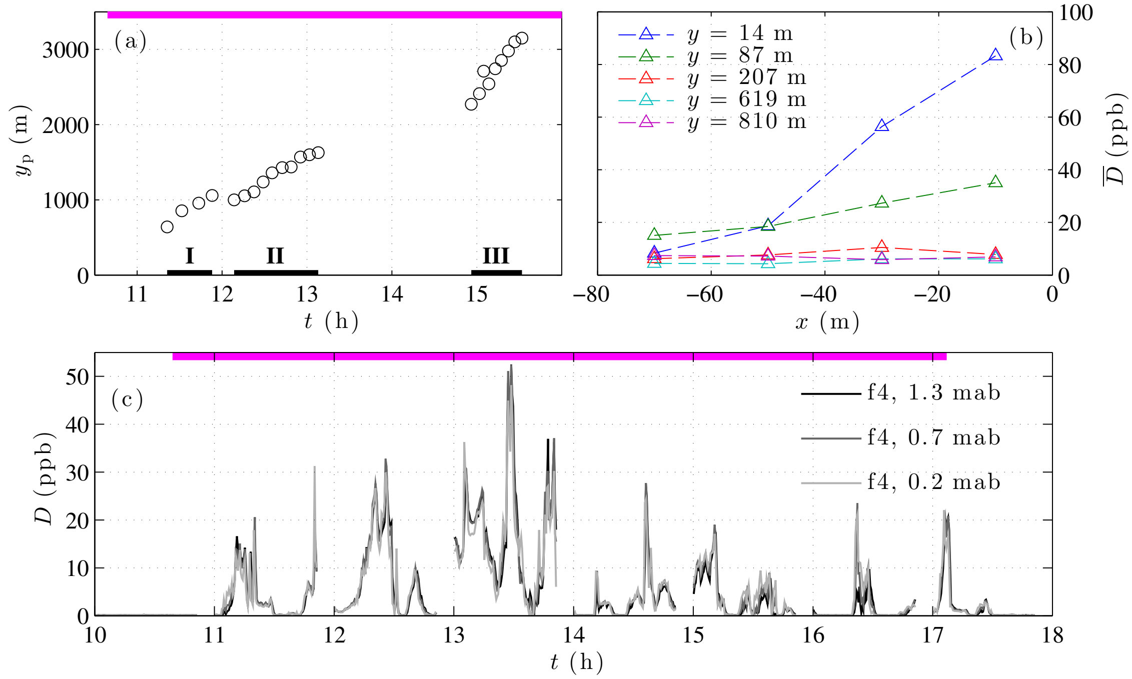

Figure 4. (a) Alongshore coordinate of dye plume leading edge y_p versus time. The determination of $y_p(t)$ is described in section 3.2. Black bars denote time periods I, II, and III. (b) Time-averaged, cross- and alongshore-binned surfzone $\overline{D}$ from jetski surface transects versus cross-shore coordinate x (see legend for alongshore locations y). The analogous dye standard deviation is $\propto \overline{D}$ at each y, and thus surfzone dye profiles for $y \geq 207$ m are cross-shore uniform. (c) Dye concentration D versus time at three ETs with different vertical elevations (mab is meters above bottom) on f4 at the seaward surfzone boundary x_b (see legend and Figure 2c). Gaps in the time series result from sampling for 51 minutes of each hour. Magenta bars in (a) and (c) indicate duration (10:39–17:07 h) of near-shoreline, continuous dye release at $y = 0$ m (star in Figures 1 and 3).

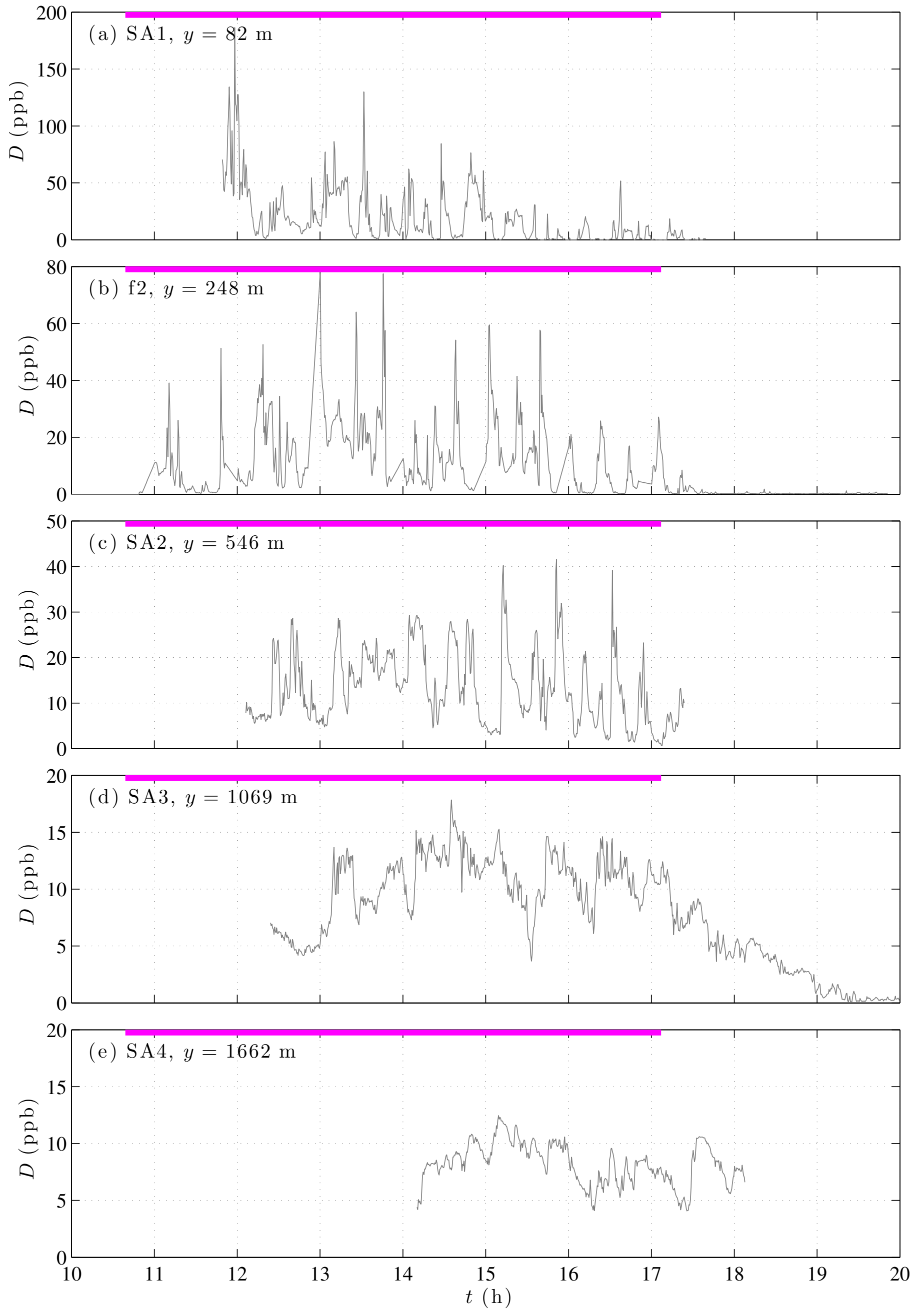

Figure 5. Dye concentration D versus time at the near-shoreline f2 and SA1-SA4 (diamond and circles, respectively, Figures 1 and 3). Alongshore location is indicated in each panel. Magenta bars indicate duration of near-shoreline, continuous dye release at $y = 0$ m (star in Figures 1 and 3). SA1-SA4 data start times correspond to instrument deployment times, not plume arrival times. Vertical axes differ.

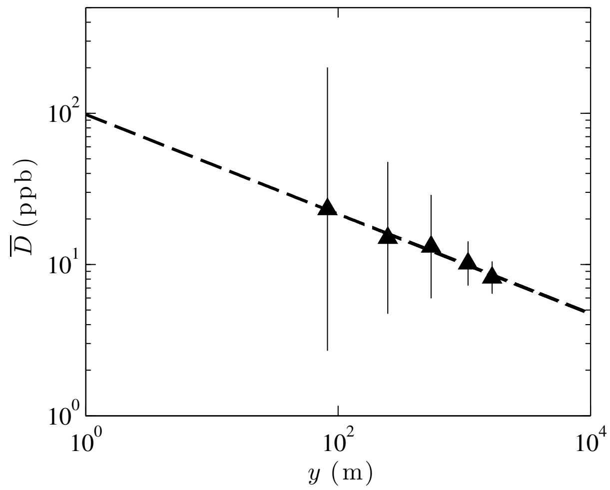

Figure 6. Mean (time-averaged) dye concentration $\overline{D}$ versus alongshore coordinate y at the near-shoreline f2 and SA1-SA4 (diamond and circles, respectively, Figures 1 and 3). Vertical bars are standard deviations about the means. Best fit line (dashed) is $\overline{D} = \overline{D}_0\,(y/y_0)^{\alpha}$, where $y_0 = 1$ m is chosen for simplicity, and best fit constants are $\overline{D}_0 = 98$ ppb and $\alpha = -0.33$.

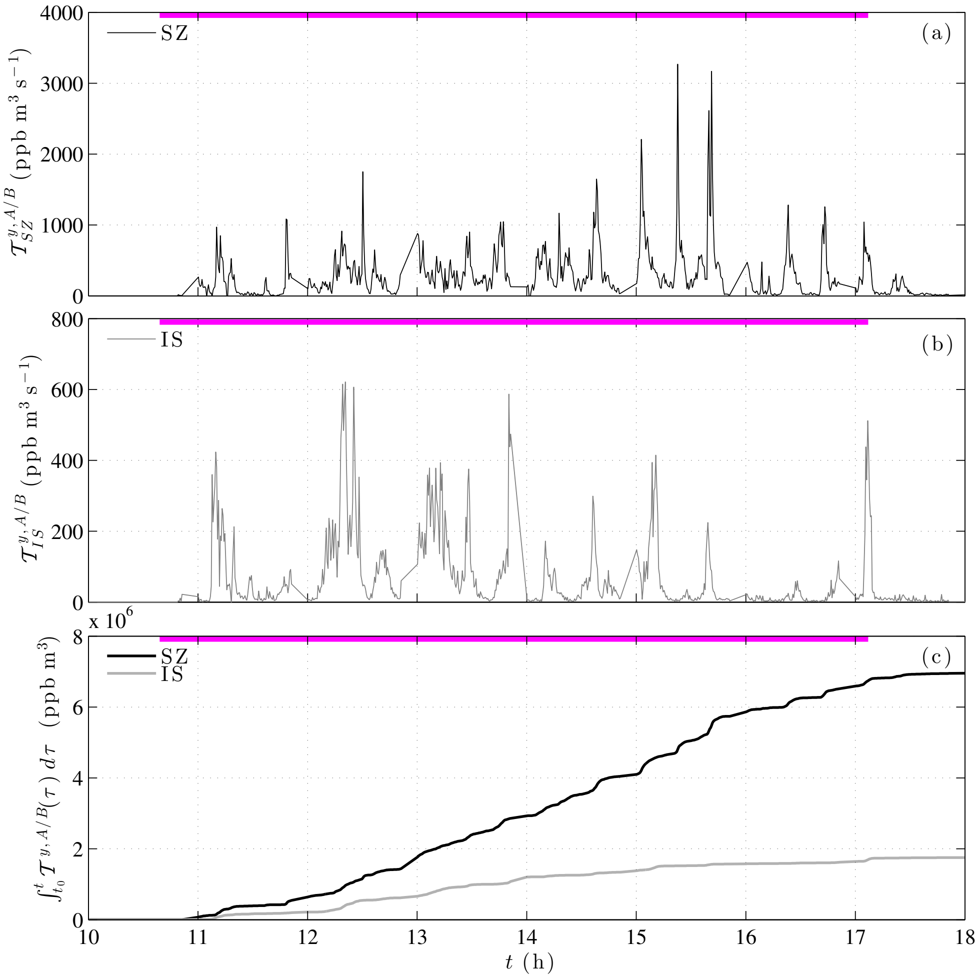

Figure 7. Time series of alongshore dye transport from region A to B in the (a) surfzone ($\mathcal{T}_{SZ}^{y,A/B}$ defined in (2)) and (b) inner-shelf ($\mathcal{T}_{IS}^{y,A/B}$ defined in (3)). Vertical axes differ. (c) Time series of cumulative (time-integrated) surfzone and inner-shelf alongshore dye transports (see legend). Magenta bars indicate duration of near-shoreline, continuous dye release (Figure 3a, star) 248 m south of the cross-shore array (Figure 3a, diamonds) that separates regions A and B . The dye release rate $Q = 512$ ppb m^3 s^{-1}, and the total dye released is 1.19×10^7 ppb m^3. In panel (c) at $t = 18{:}00$ h, the resulting cumulative dye transports normalized by the total dye released are 0.62 (surfzone) and 0.15 (inner-shelf).

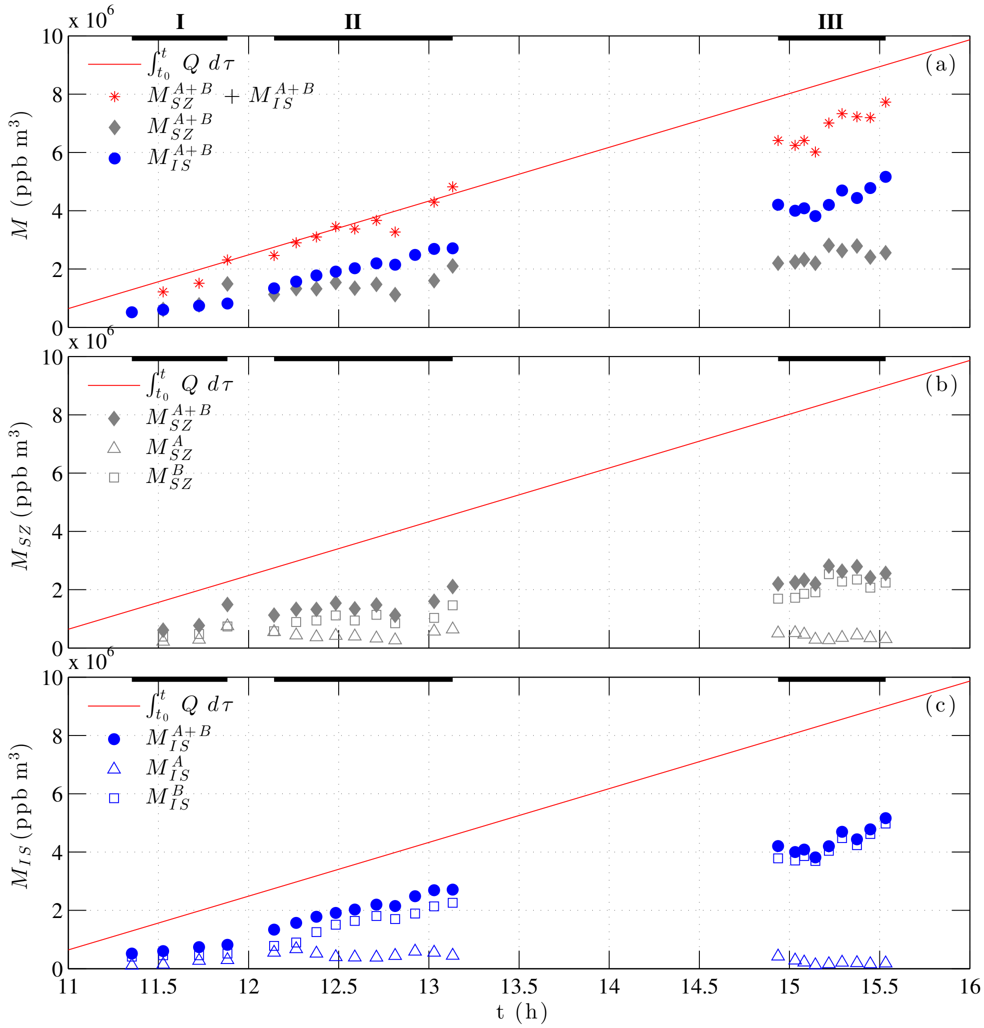

Figure 8. Dye mass M versus time. Black bars denote time periods I, II, and III. (a) Surfzone estimates M_{SZ}^{A+B} (gray) are from in situ observations, and inner-shelf estimates M_{IS}^{A+B} (blue) are from aerial observations. Red asterisks are $M_{SZ}^{A+B} + M_{IS}^{A+B}$. Red line shows the time-integrated dye released since t_0 =10:39 h ($\int_{t_0}^{t} Q\ d\tau$, where Q is the steady dye release rate). (b) Surfzone dye mass M_{SZ} versus time for the near-field region A ($y \leq 248$ m, triangles) and the far-field region B ($y > 248$ m, squares). Solid gray diamonds are M_{SZ}^{A+B}. (c) Inner-shelf dye mass M_{IS} versus time for region A (triangles) and region B (squares). Solid blue circles are M_{IS}^{A+B}. Estimation methods for M_{SZ} and M_{IS} are described in Appendix A1 and A2, respectively.

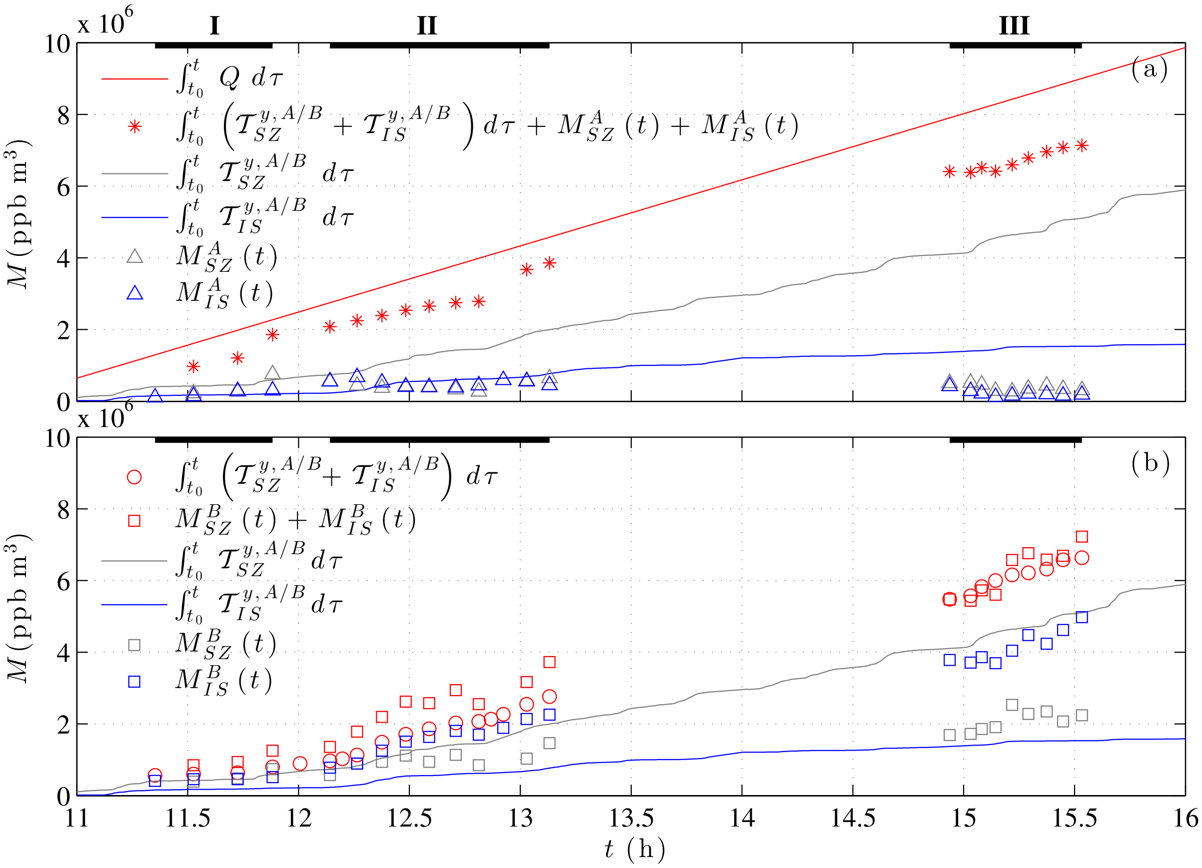

Figure 9. Dye mass balance terms versus time for (a) near-field region A ($0 < y \leq y_{\mathrm{f}} = 248$ m) and (b) far-field region B ($y > y_{\mathrm{f}} = 248$ m). See legend in each panel, and equations (7) and (8) for panels (a) and (b), respectively.

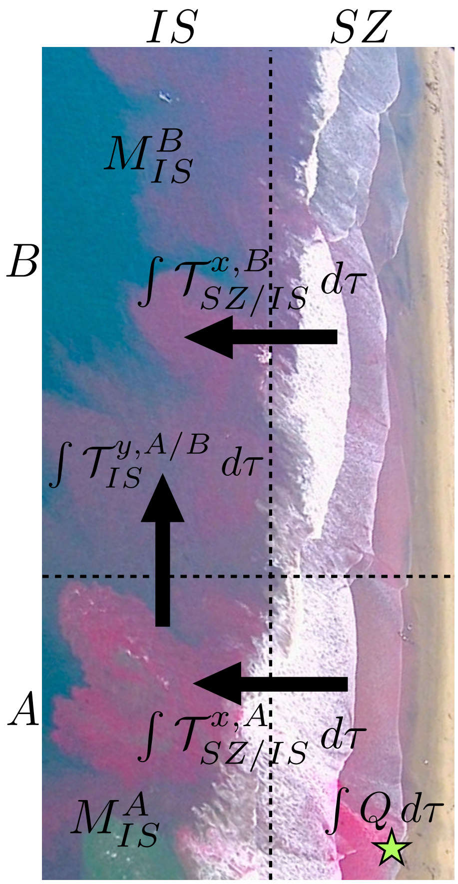

Figure 10. Planview photograph and superposed schematic of dye mass balances (9a), (9b), and (10). Star denotes location of dye released at steady rate Q.

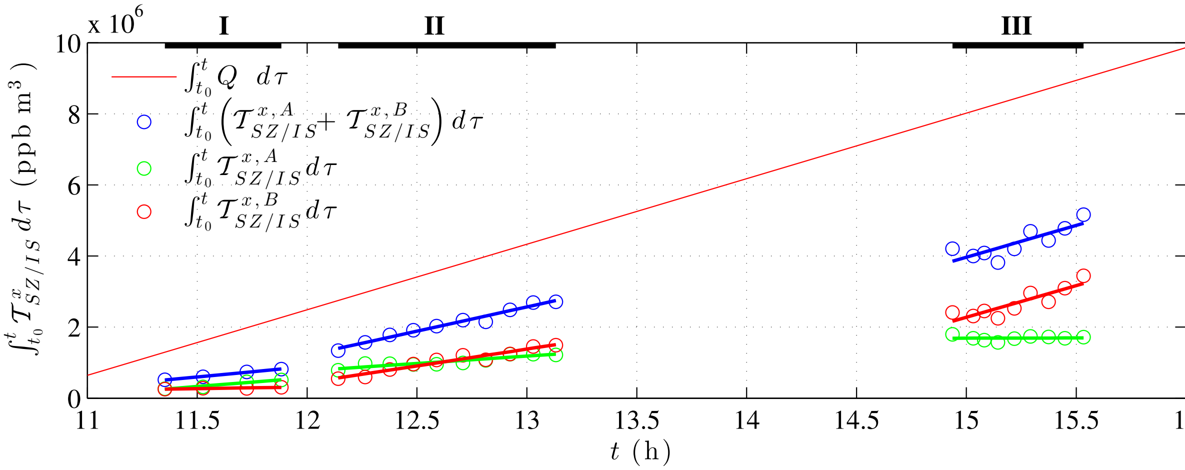

Figure 11. Time series of cumulative (time-integrated) cross-shore dye transports from the surfzone to inner-shelf (circles) inferred from inner-shelf dye mass observations M_{IS} and alongshore transport measurements $\mathcal{T}_{IS}^{y,A/B}$. See (9a), (9b), and (10). Line segments are least squares fits for each time period, and line segment slopes yield inferred cross-shore dye transports $\mathcal{T}_{SZ/IS}^{x}$. Thin red line shows the time-integrated dye released since $t_0 = $ 10:39 h.

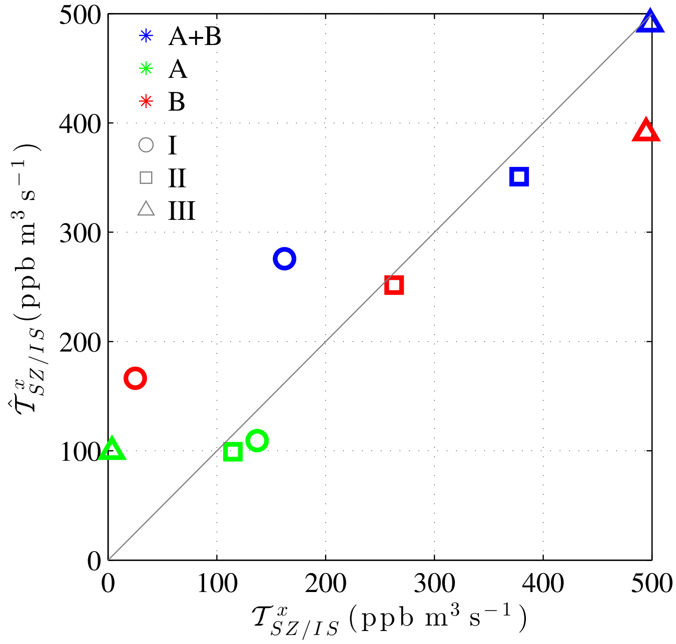

Figure 12. Parameterized cross-shore dye transport $\hat{\mathcal{T}}^x_{SZ/IS}$ versus inferred cross-shore dye transport $\mathcal{T}^x_{SZ/IS}$ for regions A, B, and A+B during periods I, II, and III (see legend). The one-to-one line is plotted in gray. The parameterized $\hat{\mathcal{T}}^x_{SZ/IS}$ follow (12a), (12b), and (13). The $\mathcal{T}^x_{SZ/IS}$ are inferred from aerial and in situ observations (see (9a), (9b), and (10)).

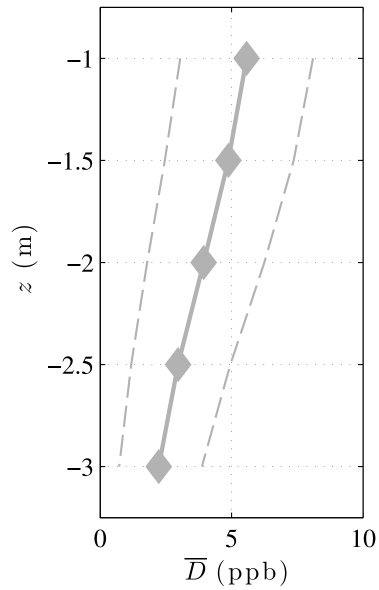

Figure 13. Mean (time- and alongshore-averaged) inner-shelf dye concentration $\overline{D}$ versus vertical coordinate z from the alongshore-towed vertical array (section 2.3.4) for data within inner-shelf dye patches ($D(x, y, z = -1 \text{ m}, t) \geq 2$ ppb). Dashed curves indicate standard deviations about the mean.

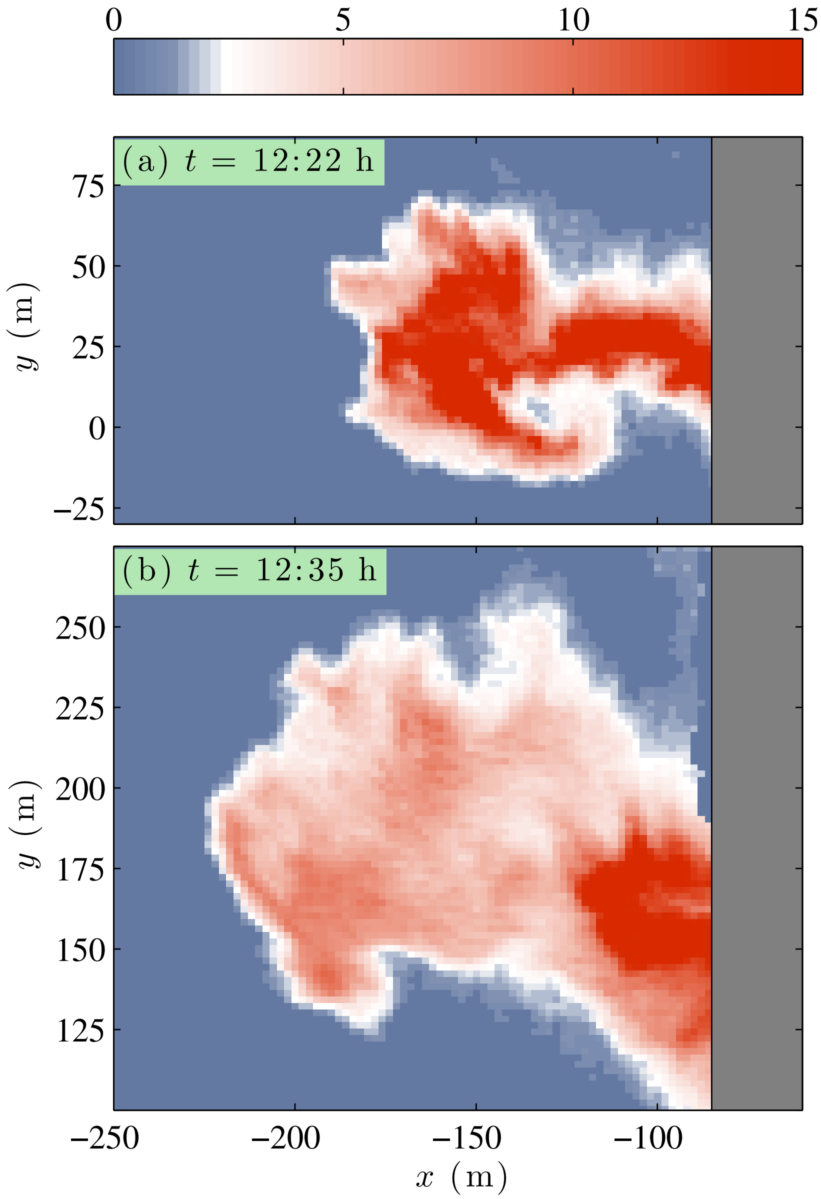

Figure 14. Aerial multispectral images of inner-shelf surface dye concentration D (ppb, see colorbar) versus cross-shore coordinate x and alongshore coordinate y for (a) a transient rip current ejection event at t = 12:22 h and (b) the subsequent dye evolution at t =12:35 h approximately 150 m downstream. Gray denotes the surfzone, largely unresolved in the aerial imagery due to foam from wave breaking. The near-shoreline dye release is at $(x, y) = (-10, 0)$ m.

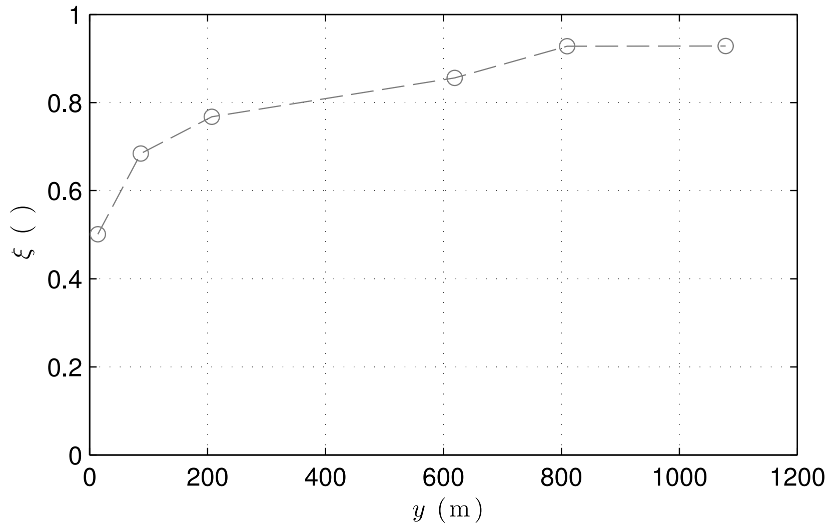

Figure 15. Surfzone dye cross-shore uniformity parameter ξ versus alongshore coordinate y (ξ is defined in (A3) and described in Appendix A1).